Cross-sectional Alignment of Polycyclic Aromatic Hydrocarbons by Anisotropic Radiation

Thiem Hoang[1,2] [ID] and A. Lazarian[3]

[1] Korea Astronomy and Space Science Institute, Daejeon 34055, Republic of Korea; thiemhoang@kasi.re.kr
[2] Korea University of Science and Technology, Daejeon, 34113, Republic of Korea
[3] Astronomy Department, University of Wisconsin, Madison, WI 53706, USA

Abstract

We study the effect of anisotropic radiation illumination on the alignment of polycyclic aromatic hydrocarbons (PAHs) and report that the cross-sectional mechanism of alignment earlier considered in terms of gas–grain interactions can also be efficient for the photon–grain interaction. We demonstrate this by first calculating the angle-dependence rotational damping and excitation coefficients by photon absorption followed by infrared emission. We then calculate the degree of PAH alignment for the different environments and physical parameters, including the illumination direction, ionization fraction, and magnetic field strength. For the reflection nebula (RN) conditions with unidirectional radiation field, we find that the degree of alignment tends to increase with increasing angle ψ between the illumination direction and the magnetic field, as a result of the decrease of the cross section of photon absorption with ψ. We calculate the polarization of spinning PAH emission using the obtained degree of alignment for the different physical parameters, assuming constant grain temperatures. We find that the polarization of spinning PAH emission from RNe can be large, between 5% and 20% at frequencies $\nu > 20$ GHz, whereas the polarization is less than 3% for photodissociation regions. In realistic conditions, the polarization is expected to be lower owing to grain temperature fluctuations and magnetic field geometry. The polarization for the diffuse cold neutral medium is rather low, below 1% at $\nu > 20$ GHz, consistent with observations by *WMAP* and *Planck*. Our results demonstrate that the RNe are the favored environment to observe the polarization of spinning dust emission and polarized mid-IR emission from PAHs.

Key words: cosmic background radiation – dust, extinction – ISM: magnetic fields – magnetic fields – polarization

1. Introduction

Polycyclic aromatic hydrocarbons (PAHs) are an important dust component of the interstellar medium (ISM; see Tielens 2008, for a review). PAH molecules are planar structures, consisting of carbon hexagonal rings and hydrogen atoms attached to their edge via valence bonds. PAHs are the leading carrier for the 2175 Å broad feature in the extinction curve (Draine 1989). Moreover, upon absorbing ultraviolet (UV) photons, PAHs reemit radiation in mid-infrared features, including 3.3, 6.2, 7.7, 8.6, 11.3, and 17 μm, due to vibrational transitions (Leger & Puget 1984; Allamandola et al. 1985; Draine & Li 2007). The evidence of PAHs is ubiquitously observed from our Galaxy (see, e.g., Tielens 2008) and external galaxies (Smith et al. 2007) to circumstellar disks around young stars (Seok & Li 2017).

Rapidly spinning PAHs emit microwave radiation via a new mechanism, so-called spinning dust (Draine & Lazarian 1998; Hoang et al. 2010). The latter is the most likely origin of anomalous microwave emission (AME) that contaminates cosmic microwave background (CMB) radiation (Kogut et al. 1996; Leitch et al. 1997).[4] Spinning dust emission can also be a source of excess microwave emission in some circumstellar disks around Herbig Ae/Be stars (Hoang et al. 2018b).

The alignment of PAH molecules can leave imprints in (1) the UV polarization of starlight at 2175 Å, (2) polarized mid-IR emission, and (3) polarized spinning dust emission. To date, only two stars exhibit the UV polarization bump, and inverse modeling in Hoang et al. (2013) found that a considerable degree of PAH alignment with the magnetic field is required to reproduce the observed polarization bump. Observational studies of polarized PAH emission are still limited. An early search by Sellgren et al. (1988) reported the detection of polarized PAH emission from the Orion ionization front, with $p \sim 0.86\% \pm 0.28\%$ for the 3.3 μm feature, although it is cautious because the ground-based measurement at 3.3 μm is very challenging owing to the atmospheric opacity. Moreover, observational studies of the AME polarization (Battistelli et al. 2006; Mason et al. 2009; Dickinson et al. 2011; Battistelli et al. 2015) only found the upper limits, with the polarization level between 1% and 5%. An upper limit of 1% is also reported in various studies (see López-Caraballo et al. 2011; Rubiño-Martín et al. 2012; Génova-Santos et al. 2017). Therefore, a physical prediction for polarized spinning dust emission is crucially important for interpretation of the observed AME polarization.

Very recently, Zhang et al. (2017) detected the polarization at 11.3 μm from the MWC 1080 nebula. The measured polarization of $1.9\% \pm 0.2\%$ can be successfully explained when PAHs can be aligned with the magnetic field to a degree of 10%. Yet an underlying mechanism of PAH alignment is still unclear.

The theory of grain alignment (see Lazarian et al. 2015, for a review) was developed to mainly explain the alignment of large classical grains (i.e., above ~0.01 μm) rather than nanoparticles.

---

[4] PAH molecules definitely emit microwave radiation. The efficiency of their emission depends on the dipole moments of the molecules, and the latter parameter is somewhat uncertain. Therefore, we do not know exactly what percentage of microwave radiation has the PAH origin. Alternative sources of AME include magneto-dipole emission from strongly magnetized classical large grains (Draine & Lazarian 1999; Draine & Hensley 2013), magnetic nanoparticles (Hoang & Lazarian 2016a), and silicate spinning nanoparticles (Hoang et al. 2016; Hensley & Draine 2017).

For instance, the analytical theory of radiative torques (RATs) acting on ordinary paramagnetic grains (Lazarian & Hoang 2007b; Hoang & Lazarian 2008) and the theory of RATs acting on grains with magnetic inclusions (Lazarian & Hoang 2008; Hoang & Lazarian 2016b) do not predict any alignment of nanoparticles, as the efficiency of RATs decreases rapidly as the size of the grain gets much smaller than the radiation wavelength. The mechanical alignment arising from the gas–grain interactions can occur, but for both the alignment of nonhelical grains (see Lazarian 1997a) and the mechanical alignment of helical grains (Lazarian & Hoang 2007a; Das & Weingartner 2016; Hoang et al. 2018a), relatively high drift velocities of gas and dust are required. The mechanisms of dust acceleration involving magnetohydrodynamic (MHD) turbulence (see Hoang et al. 2012, and references therein), as well as due to Coulomb interaction of fluctuating charges on grains (Hoang & Lazarian 2012), do not provide sufficiently high drift velocities.

Lazarian & Draine (2000) first suggest that rapidly spinning nanoparticles can be weakly aligned by *resonance paramagnetic relaxation*, a modified version of the Davis–Greenstein mechanism (Davis & Greenstein 1951) that works in rapidly spinning tiny grains. Numerical calculations in Hoang et al. (2014) found that resonance relaxation can enable PAHs to be aligned up to a degree of ∼10%. We believe that this mechanism provides a viable candidate for nanoparticle alignment in terms of both PAHs and silicate nanoparticles in spite of recent controversy about its efficiency (see Draine & Hensley 2016).[5] Theoretical calculations in Hoang (2017) found that if PAHs are aligned with the magnetic field by paramagnetic resonance mechanism, their mid-IR emission can be polarized to a few percent for the RN conditions. The remaining question is, are there any alternative processes that can align PAHs?

The history of grain alignment ideas (see Lazarian 2003, for a review) is rich, and various ideas have been tested. In particular, in Lazarian (1995a), the cross-sectional alignment mechanism was proposed as a means of aligning disk-like grains. The essence of the mechanism is that the rate of the diffusion of the grain angular momentum can change depending on the cross section that the planar grain exposes to the flow of atoms. This mechanism relies on the effect that the grain would stay in the position that minimizes its cross section (see also Lazarian & Efroimsky 1996). PAH molecules likely exhibit this type of planar geometry. However, instead of atoms whose arrival and subsequent evaporation would induce angular momentum diffusion, it is more promising to consider the flow of anisotropic radiation. Therefore, in this paper we explore the cross-sectional alignment of PAHs by anisotropic radiation.

Previous studies for alignment of nanoparticles were carried out for the diffuse cold neutral medium (CNM; e.g., Lazarian & Draine 2000; Hoang et al. 2013, 2014; Draine & Hensley 2016), where the radiation field can be considered isotropic.

For the conditions of reflection nebulae (RNe) and photo-dissociation regions (PDRs), the unidirectional illumination is present; thus, the cross-sectional alignment mechanism is perhaps important.

The structure of our paper is as follows. Section 2 describes the basic physics of PAHs, including magnetic properties and internal relaxation. In Section 3 we present the rotational damping and excitation for anisotropic illumination and calculate the averaged diffusion coefficients over internal thermal fluctuations. In Section 4, we describe alignment physics and the numerical method to compute the degree of PAH alignment. Section 5 presents our obtained results on PAH alignment for the various environment conditions and physical parameters. In Section 6, we compute the polarization of spinning dust emission using the resulting degree of alignment for RNe, PDRs, and CNM. Discussion and summary are presented in Section 8.

2. PAH Physics and Internal Relaxation

2.1. PAH Geometry

Let us consider a PAH molecule that has an axisymmetric shape with the symmetry axis $\hat{a}_1$ and $\hat{a}_2\hat{a}_3$ lying in the plane. The shape is assumed to be disk-like for the smallest PAHs and an oblate spheroid of axial ratio $s < 1$ for large PAHs. The effective size of the molecule is defined as the radius of the sphere having the same volume and is given by $a = a_2 s^{1/3}$, where a_1 and a_2 are the lengths of the semimajor and semiminor axes, respectively. The transition from disk-like to oblate spheroid is set to be at $a = 6\,\text{Å}$ (Draine & Lazarian 1998; Hoang et al. 2010 (hereafter HDL10). Let $I_\parallel$ and $I_\perp$ be the moments of inertia along $\hat{a}_1$ and $\hat{a}_2$, and $h_a = I_\parallel/I_\perp$ (see, e.g., Hoang et al. 2016, for their formulae).

2.2. Magnetic Properties

Ideal PAHs are expected to have rather low paramagnetic susceptibility owing to H nuclear spin (Jones & Spitzer 1967). However, astrophysical PAHs are likely magnetized thanks to the presence of free radicals, paramagnetic carbon rings, or adsorption of ions (see Lazarian & Draine 2000).

Over the past decade, significant progress has been made in research on magnetism of graphene, providing important insight into magnetism of PAHs. For instance, Yazyev & Helm (2007) suggested that graphene can be magnetized by defects in carbon rings and adsorption of hydrogen atoms to the surface. The vacancy of carbon atoms from the carbon rings creates unpaired electrons, giving rise to the magnetization of graphene (Yazyev & Helm 2007). Also, the adsorption of a hydrogen atom induces magnetic ordering (see Lehtinen et al. 2004), which is detected in a recent experiment (González-Herrero et al. 2016). In the ISM, the defects of PAHs can be triggered by bombardment of cosmic rays. All in all, astrophysical PAHs are likely paramagnetic. Let f_p be the fraction f_p of paramagnetic atoms in the grain, and we take $f_p = 0.01$ for calculations of PAH magnetic susceptibility, as in previous works (see Hoang et al. 2014, for details).

2.3. Internal Relaxation and Thermal Fluctuations

Barnett (1915) first pointed out that a rotating paramagnetic body can get magnetized with the magnetic moment along the grain angular velocity. Later, Dolginov & Mytrophanov (1976)

---

[5] Draine & Hensley (2016) pointed out that the quantization effect may significantly suppress the alignment of nanoparticles because the vibrational energy levels are too broad compared to the intrinsic broadening width, freezing the energy transfer from the rotational system to the vibrational system. This can lead to negligible polarization of spinning dust emission. However, the treatment of quantum suppression in Draine & Hensley (2016) is perhaps incomplete because the effect of Raman phonon scattering discussed in Lazarian & Draine (2000) in relation to the paramagnetic relaxation is disregarded.

introduced the magnetization via the Barnett effect for dust grains and considered its consequence on grain alignment.

Purcell ([1979]) realized that the precession of $\boldsymbol{\omega}$ coupled to $\boldsymbol{\mu}_{\mathrm{Bar}}$ around the grain symmetry axis $\hat{\boldsymbol{a}}_1$ produces a rotating magnetization component within the grain-body coordinates. As a result, the grain rotational energy is gradually dissipated until $\boldsymbol{\omega}$ becomes aligned with $\hat{\boldsymbol{a}}_1$—an effect that Purcell termed "Barnett relaxation."

Internal relaxation involves the transfer of grain rotational energy to vibrational modes. Naturally, if the grain has nonzero vibrational energy, energy can also be transferred from the vibrational modes to the rotational energy (Jones & Spitzer [1967]). For an isolated grain, a small amount of energy gained from the vibrational modes can induce fluctuations of the rotational energy E_{rot} when the grain angular momentum $\boldsymbol{J}$ is conserved (Lazarian [1994]). Over time, the fluctuations in E_{rot} establish a local thermal equilibrium (LTE).

The rotational energy is $E_{\mathrm{rot}} = J^2[1 + (h_a - 1)\sin^2\theta]/2I_{\parallel}$, where θ is the angle between $\hat{\boldsymbol{a}}_1$ and $\boldsymbol{J}$. Thermal fluctuations of θ can be described by the Boltzmann distribution (Lazarian & Roberge [1997]):

$$f_{\mathrm{LTE}}(\theta, J) = Z \exp\left(-\frac{J^2}{2I_{\parallel}k_B T_d}[1 + (h_a - 1)\sin^2\theta]\right), \quad (1)$$

where Z is the normalization constant such that $\int_0^\pi f_{\mathrm{LTE}}(\theta, J)\sin\theta d\theta = 1$, and T_d is the internal alignment temperature above which the vibrational–rotational energy exchange is still effective.

The temperature of small PAHs undergoes strong fluctuations due to stochastic heating by UV photons (Purcell [1976]; Guhathakurta & Draine [1989]; Draine & Li [2001]). In this paper, to capture the effect of anisotropic illumination on PAH alignment, T_d is assumed to be constant, and a detailed discussion of its effect will be presented in Section [7.4].

3. Rotational Damping and Excitation by Anisotropic Radiation

3.1. Rotational Damping and Excitation Coefficients

The dimensionless damping and excitation coefficients, F and G, are defined as

$$F_{j,r} = -\frac{\tau_{\mathrm{H},r}}{\omega_r}\frac{d\omega_r}{dt}, \quad (2)$$

$$G_{j,r} = \frac{\tau_{\mathrm{H},r}}{2k_B T_{\mathrm{gas}}}\frac{I_r d\omega_r^2}{dt}, \quad (3)$$

where $r = \parallel, \perp$ denotes the rotation parallel and perpendicular to the grain symmetry axis; $j = n, i, p$, and IR denote collisions of the grain with neutral, ion, plasma–grain interactions, and infrared emission; $\tau_{\mathrm{H},r}$ is the damping time of the grain in a purely H I gas of temperature T_{gas}; and I_r is the moment of inertia along the axis r (see also Hoang et al. [2010]).

We start by considering photon absorption of a PAH molecule in an isotropic radiation field. Thus, the rate of photon absorption is given by

$$\dot{N}_{\mathrm{abs},0} = \int C_{\mathrm{abs}}\frac{cu_\nu}{h\nu}d\nu, \quad (4)$$

where u_ν is the spectral energy density of the isotropic interstellar radiation in the solar neighborhood with the total
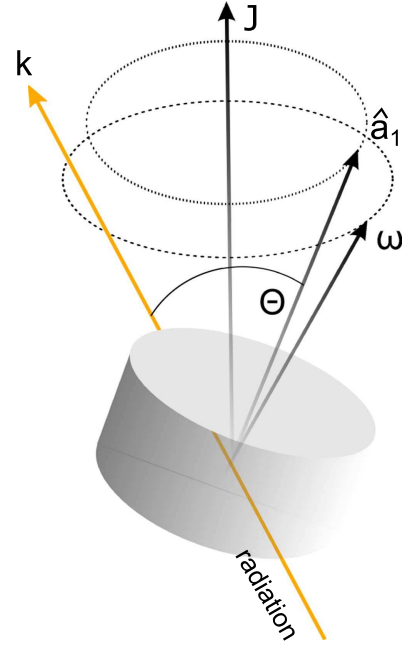
Figure 1. Schematic of a disk-like PAH molecule with the symmetry axis $\hat{\boldsymbol{a}}_1$, rotating with angular momentum $\boldsymbol{J}$, illuminated by the radiation along the direction $\boldsymbol{k}$. The cross section of photon absorption is determined by the angle Θ.

energy density $u_{\mathrm{rad}}^{\mathrm{M83}} = 8.63 \times 10^{-13}\,\mathrm{erg\,cm^{-3}}$ from Mathis et al. ([1983]), and C_{abs} is the absorption cross section from PAHs, taken from Draine & Li ([2001]).

Let us now consider an anisotropic radiation field of anisotropy degree γ, with the spectral energy density $u_\nu = U u_\nu^{\mathrm{M83}}$, where U is the dimensionless scaling factor. Let $\hat{\boldsymbol{z}}_k$ be the anisotropic direction of the radiation that makes an angle Θ with the PAH symmetry axis $\hat{\boldsymbol{a}}_1$ (see Figure [1]). To account for the effect of anisotropic illumination, a window Ψ function is introduced (see [HDL10]):

$$\dot{N}_{\mathrm{abs}} = U\Psi(\Theta)\dot{N}_{\mathrm{abs},0}, \quad (5)$$

where

$$\Psi(\Theta) = (1 - \gamma) + \frac{3}{4}(1 + \cos^2\Theta)\gamma. \quad (6)$$

For an isotropic radiation field, $\gamma = 0$, and the function $\Psi(\Theta)$ returns to unity. For a unidirectional radiation ($\gamma = 1$), the absorption cross section at $\Theta = 0$ is twice that at $\Psi = \pi/2$ (Sironi & Draine [2009]; Hoang [2017]).

Let $P_{m,\nu,0}$ be the time-averaged emission power in mode m at frequency ν due to the absorption of isotropic radiation. Then the total rate of photon emission in the anisotropic case is

$$\dot{N}_m = \Psi(\Theta)\dot{N}_{m,0} = \Psi(\Theta)\int_0^\infty \frac{P_{m,\nu,0}}{h\nu}d\nu, \quad (7)$$

where $m = \mathrm{ip}$ (in-plane) or $m = \mathrm{oop}$ (out-of-plane) emission mode. The averaged wavelength of emission is $\langle\lambda\rangle_m = \int_0^\infty\left(\frac{\lambda P_{m,\nu,0}}{h\nu}d\nu\right)/\dot{N}_{m,0}$.

The parallel and perpendicular components of the damping and excitation coefficients induced by photon absorption

followed by infrared emission are then given by

$$F_{\mathrm{IR},\|,0} = \frac{3\hbar}{2\pi I_\| c}\dot{N}_{\mathrm{ip},0}\langle\lambda\rangle_{\mathrm{ip}}\tau_{\mathrm{H},\|}, \qquad (8)$$

$$F_{\mathrm{IR},\perp,0} = \frac{3\hbar}{2\pi I_\perp c}\left[\frac{1}{2}\dot{N}_{\mathrm{ip},0}\langle\lambda\rangle_{\mathrm{ip}} + \dot{N}_{\mathrm{oop},0}\langle\lambda_{\mathrm{oop}}\rangle\right]\tau_{\mathrm{H},\perp}, \qquad (9)$$

and

$$G_{\mathrm{IR},\|,0} = \frac{1}{2}\frac{[\dot{N}_{\mathrm{abs},0} + \dot{N}_{\mathrm{ip},0}]2\hbar^2}{2I_\| k_{\mathrm{B}}T_{\mathrm{gas}}}\tau_{\mathrm{H},\|}, \qquad (10)$$

$$G_{\mathrm{IR},\perp,0} = \frac{1}{2}\frac{\left[\dot{N}_{\mathrm{oop},0} + \frac{1}{2}(\dot{N}_{\mathrm{abs},0} + \dot{N}_{\mathrm{ip},0})\right]2\hbar^2}{2I_\perp k_{\mathrm{B}}T_{\mathrm{gas}}}\tau_{\mathrm{H},\perp}, \qquad (11)$$

where the recoil of angular momentum $L = \hbar\sqrt{j(j+1)} = \sqrt{2}\,\hbar$ has been used.

For an anisotropic radiation field, the damping and excitation coefficients become

$$F_{\mathrm{IR},j}(\Theta) = U\Psi(\Theta)F_{\mathrm{IR},j,0}, \qquad (12)$$

$$G_{\mathrm{IR},j}(\Theta) = U\Psi(\Theta)G_{\mathrm{IR},j,0}, \qquad (13)$$

where $j = \|, \perp$. The damping and excitation coefficients are thus maximum for $\Theta = 0$ and minimum for $\Theta = \pi/2$.

The total IR coefficients are given by $F_{\mathrm{IR,neu}}f_0 + (1 - f_0)F_{\mathrm{IR,ion}}$, where neu and ion denote neutral PAH and ionized PAH, respectively (both positive and negative charge states). Here we assume neutral PAHs ($f_0 = 1$) in calculations of F_{IR} and G_{IR}.

To compute $F_{\mathrm{IR},j}$ and $G_{\mathrm{IR},j}$ induced by anisotropic radiation with Equations (12) and (13), we take $\langle\lambda\rangle$, $\dot{N}_{\mathrm{ip},0}$, $\dot{N}_{\mathrm{oop},0}$, and $\dot{N}_{\mathrm{abs},0}$ computed in HDL10. For circumstellar regions or RNe, we assume that the spectrum of radiation is similar to that of the standard local interstellar radiation field (ISRF; Mathis et al. 1983), but the strength of the radiation is described by the parameter U. Other F and G coefficients are calculated as in HDL10, where the charge distribution of nanoparticles arising from collisional charging and the photoelectric effect is computed as in Hoang & Lazarian (2012).

3.2. Averaging the Damping and Diffusion Coefficients over Thermal Fluctuations

For a fixed angular momentum, the $F_{\mathrm{IR}}(\Theta)$ and $G_{\mathrm{IR}}(\Theta)$ coefficients fluctuate as a result of the fluctuations of the angle θ between $\hat{a}_1$ and $\boldsymbol{J}$. To consider the effect of the coefficients on the alignment, we first need to transform the coefficients to the lab system, and then we average it over the thermal fluctuations.

3.2.1. Transformation

To study the alignment of the grain angular momentum $\boldsymbol{J}$ with the ambient magnetic field $\boldsymbol{B}$, we consider an inertial lab coordinate system denoted by unit vectors $\hat{x}_B\hat{y}_B\hat{z}_B$ such that $\hat{z}_B\|\boldsymbol{B}$ (see Figure 2, right panel).

The coefficients $F_{\mathrm{IR}}(\Theta)$ and $G_{\mathrm{IR}}(\Theta)$ depend on the instantaneous orientation of the PAH molecule in the lab system. Thus, first, we have to transform these coefficients from the grain body to the lab reference frame.

For the diffusion coefficients, $B_{ij}^b = \langle\Delta J_i^b\Delta J_j^b/\Delta t\rangle$ with $B_{ij}^b = 0$ for $i \neq j$. These diffusion coefficients are related to the

dimensionless excitation coefficients G_j as follows:

$$B_{j,zz}^b = B_{j,\|}^b = \frac{2I_\| k_{\mathrm{B}}T_{\mathrm{gas}}}{\tau_{\mathrm{H},\|}}G_{j,\|}, \qquad (14)$$

$$B_{j,xx}^b = B_{yy}^b = B_{j,\perp}^b = \frac{2I_\perp k_{\mathrm{B}}T_{\mathrm{gas}}}{\tau_{\mathrm{H},\perp}}G_{j,\perp}, \qquad (15)$$

where $j = n$, ion, p, IR denotes the various interaction processes.

The transformation of the diffusion coefficients from the body frame to the lab system is carried out as in HDL10 (see also Lazarian 1997b), and we obtain $A_{j,i}$ and $B_{j,ii}$ in the lab system for all processes j:

$$B_{j,ii} = B_{j,\|}^b g_{i,\|} + B_{j,\perp}^b g_{i,\perp}, \qquad (16)$$

where $g_{i,\|}$ and $g_{i,\perp}$ are the transformation functions, which depend on j (see Appendix A for details).

In dimensionless units of $J' = J/I_\|\omega_{T,\|}$ and $t' = t/\tau_{\mathrm{H},\|}$, the coefficients are denoted with a prime. Using Equation (16), the dimensionless coefficients for IR emission at a given orientation of $\boldsymbol{J}$ described by (ξ, ϕ, ψ) can be written as

$$A_{\mathrm{IR},i}'(\boldsymbol{J}, \theta, \zeta) = F_{\mathrm{IR},\|}(\Theta)(\cos^2\theta + \gamma_{\mathrm{H}}\sin^2\theta), \qquad (17)$$

$$B_{\mathrm{IR},ii}'(\boldsymbol{J}, \theta, \zeta) = G_{\mathrm{IR},\|}(\Theta)g_{i,\|} + G_{\mathrm{IR},\perp}(\Theta)g_{i,\perp}\left(\frac{\epsilon_{\mathrm{H}}}{h_a}\right), \qquad (18)$$

where $i = x, z$, $\epsilon_{\mathrm{H}} = \tau_{\mathrm{H},\|}/\tau_{\mathrm{H},\perp}$, $\gamma_{\mathrm{H}} = (F_{\mathrm{IR},\perp}/F_{\mathrm{IR},\|})\epsilon_{\mathrm{H}}$, and the angle θ, ζ describes the orientation of $\hat{a}_1$ with $\boldsymbol{J}$ (see Appendix A).

The angle Θ between the illumination direction and the grain symmetry axis is determined by

$$\cos\Theta = \hat{a}_1.\hat{z}_k, \qquad (19)$$

which is a function of five angles (ζ, θ, ϕ, ξ, ψ) (see Equations (49)–(52)).

3.2.2. Averaging over Thermal Fluctuations

The alignment of PAHs with the magnetic field due to magnetic relaxation occurs on a timescale much longer than the rotation period of the PAH around its symmetry axis, the internal relaxation. Therefore, we can average the diffusion coefficients over these fast processes.

First, we average $A_{\mathrm{IR}}'(\boldsymbol{J}, \theta, \zeta)$ and $B_{\mathrm{IR},ii}'(\boldsymbol{J}, \theta, \zeta)$ over the rotation angle ζ of the grain around $\hat{a}_1$. Then, we average the obtained coefficients over the internal thermal fluctuations. The resulting averaged diffusion coefficients are equal to
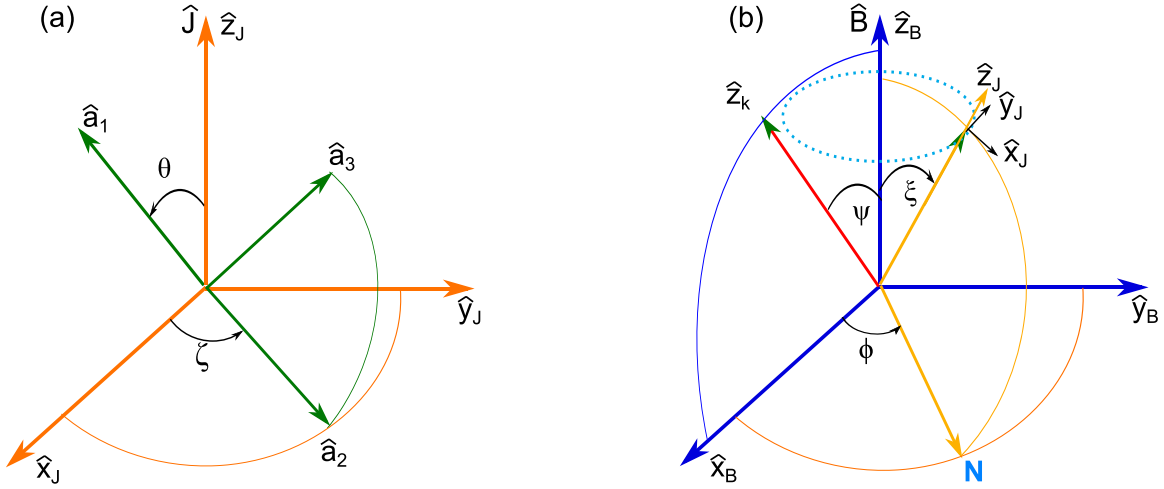
$$\bar{A}_{\mathrm{IR},i}'(J, \xi, \phi, \psi) = \frac{1}{2\pi}\int_0^\pi d\theta \int_0^{2\pi} d\zeta A_{\mathrm{IR},i}'(\boldsymbol{J}, \theta, \zeta)f_{\mathrm{LTE}}, \qquad (20)$$

$$\bar{B}_{\mathrm{IR},ii}'(J, \xi, \phi, \psi) = \frac{1}{2\pi}\int_0^\pi d\theta \int_0^{2\pi} d\zeta B_{\mathrm{IR},ii}'(\boldsymbol{J}, \theta, \zeta)f_{\mathrm{LTE}}, \qquad (21)$$

where the integration over ζ can be separated from θ owing to the much faster rotation around $\hat{a}_1$.

Finally, we average over the Larmor precession:

$$\langle B_{\mathrm{IR},ii}'\rangle(J, \xi, \psi) = \frac{1}{2\pi}\int d\phi \bar{B}_{\mathrm{IR},ii}'(J, \xi, \phi, \psi), \qquad (22)$$

Figure 2. Left panel: orientation of an axisymmetric grain described by three principal axes $\hat{a}_1\hat{a}_2\hat{a}_3$ in the coordinate system defined by J. The axis $\hat{a}_2$ is chosen along the line of node. Right panel: orientation of J in the coordinate system defined by the magnetic field $B\|\hat{z}_B$, $\hat{z}_J\|J$, $\hat{x}_J \equiv \hat{\xi}$, and $\hat{y}_J \equiv \hat{\phi}$.

where $ii = xx$, yy, zz. The Larmor precession averaging is straightforward by replacing $\cos^2\phi$ with $\langle\cos^2\phi\rangle = \int_0^{2\pi} d\phi\,\cos^2\phi/2\pi = 1/2$ and $\langle\sin^2\phi\rangle = 1/2$.

3.2.3. Numerical Results

For each radiation direction ψ, we compute the averaged coefficients $\langle A'_{\rm IR}\rangle$ and $\langle B'_{\rm IR}\rangle$ as functions of $J' = 0.1$–10 and $\xi = 0 - \pi$. Then, we will use the tabulated data $\langle A'_{\rm IR}\rangle(J, \xi)$ and $\langle B'_{\rm IR}\rangle(J, \xi)$ for solving the equations of motion in Section 4.2.

Figure 3 (top panels) shows $\langle A'_{\rm IR}\rangle(J, \xi)$ and $\langle B'_{\rm IR}\rangle(J, \xi)$ as a function of the angle ξ for several values of J and $\psi = 0°$. For the case of subthermal rotation (i.e., $J' \leqslant 0.5$), $\langle A'_{\rm IR}\rangle$ is essentially similar for the different ξ because the strong thermal fluctuations result in nearly isotropic distribution of the PAH orientation in the space. For $J' \gg 1$, the thermal fluctuations are very weak owing to suprathermal rotation; thus, the PAH is spinning with $\hat{a}_1$ aligned with J. As a result, $\langle A'_{\rm IR}\rangle$ is maximum at $\xi = 0, \pi$, i.e., when the PAH plane is perpendicular to the incident radiation such that the photon absorption cross section is maximum. The coefficients are minimum at $\xi = \pi/2$, i.e., depending on the anisotropy direction. For $\psi = 60°$, the maximum coefficient occurs at $\cos\xi = \pi/2$, shifted from $\cos\xi = \pm 1$.

4. PAH Alignment by Anisotropic Radiation Field

4.1. Resonance Paramagnetic Relaxation

Davis & Greenstein (1951) suggested that a paramagnetic grain rotating with angular velocity ω in an external magnetic field B experiences paramagnetic relaxation owing to the lag of magnetization, which dissipates the grain rotational energy into heat. This results in the gradual alignment of ω and J with the magnetic field until the rotational energy is minimum.

For ultrasmall grains, such as PAHs, the classical Davis–Greenstein relaxation is suppressed because the rotation time is shorter than the electron–electron spin relaxation time τ_2 (see Hoang et al. 2014). Yet, such nanoparticles can be partially aligned by resonance paramagnetic relaxation that originates from the splitting of the rotational energy (Lazarian & Draine 2000). Numerical calculations in Hoang et al. (2014) showed

that PAHs can be aligned by resonance paramagnetic relaxation with the degree $Q_J \sim 0.05$–0.15 depending on T_0 and the magnetic field strength. Such a considerable degree of external alignment will produce anisotropy distribution of the angular momentum in the space, enhancing the polarization of PAH emission features. Hoang & Lazarian (2016a) extended alignment calculations for iron nanoparticles and nanosilicates.

4.2. Numerical Method

To study the alignment of PAHs with the magnetic field, we solve the Langevin equations (LEs):

$$dJ_i = A_i dt + \sqrt{B_{ii}}\,dW_i \text{ for } i = 1, 2, 3, \tag{23}$$

where dW_i are the random variables drawn from a normal distribution with zero mean and variance $\langle dW_i^2\rangle = dt$, and $A_i = \langle\Delta J_i/\Delta t\rangle$ and $B_{ii} = \langle(\Delta J_i)^2/\Delta t\rangle$ are the damping and diffusion coefficients defined in the lab $\hat{e}_1\hat{e}_2\hat{e}_3$ system, respectively. Here $\hat{e}_1 \equiv \hat{z}_B$, $\hat{e}_2 \equiv \hat{x}_B$, and $\hat{e}_3 \equiv \hat{y}_B$ (see Figure 2, right panel).

To incorporate paramagnetic relaxation, we add a damping term $-J_{2,3}/\tau_{\rm mag}$ to $A_{2,3}$ and an excitation term $B_{\rm mag,22} = B_{\rm mag,33}$ to B_{22} and B_{33}, respectively. In the dimensionless units of J' and t', Equation (23) becomes

$$dJ'_i = A'_i dt' + \sqrt{B'_{ii}}\,dw'_i \text{ for } i = 1, 2, 3, \tag{24}$$
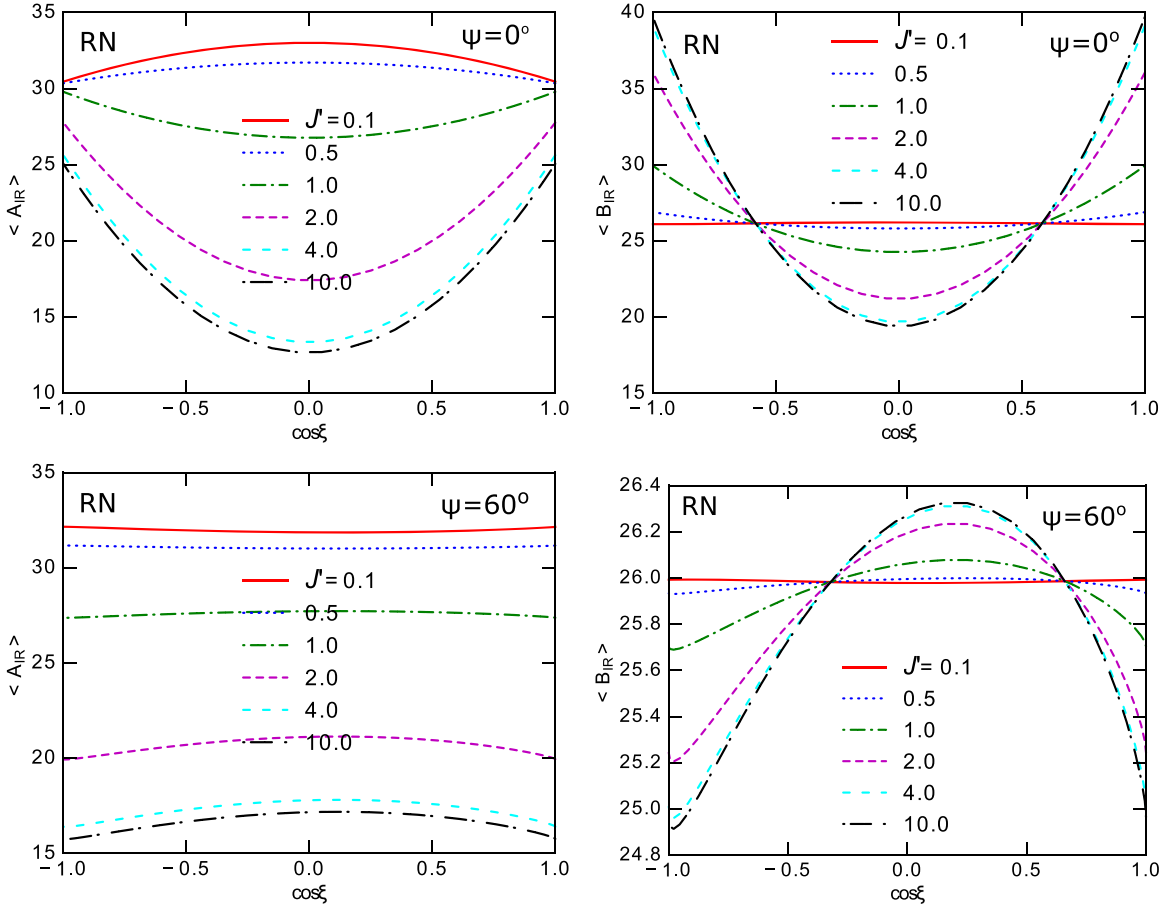
where $\langle dw_i'^2\rangle = dt'$ and

$$A'_i = -J'_i\left[\frac{1}{\tau'_{\rm gas,eff}} + \delta_m(1 - \delta_{1i})\right] - \frac{2}{3}\frac{J_i'^3}{\tau'_{\rm ed,eff}}, \tag{25}$$

$$B'_{ii} = \frac{B_{ii}}{2I_\|k_B T_{\rm gas}}\tau_{\rm H,\|} + \frac{T_d}{T_{\rm gas}}\delta_{\rm mag}(1 - \delta_{1i}). \tag{26}$$

Above, $\delta_{1i} = 1$ for $i = 1$ and $\delta_{1i} = 0$ for $i \neq 1$, and

$$\tau'_{\rm gas,eff} = \frac{\tau_{\rm gas,eff}}{\tau_{\rm H,\|}}, \tau'_{\rm ed,eff} = \frac{\tau_{\rm ed,eff}}{\tau_{\rm H,\|}}, \tag{27}$$

where $\tau_{\rm gas,eff}$ and $\tau_{\rm ed,eff}$ are the effective damping times due to dust–gas interactions and electric dipole emission (see Equation E4 in HDL10).

Figure 3. Averaged IR damping coefficient (left panel) and excitation coefficient (right panel) vs. $\cos\xi$ for the different values of grain angular momentum J' in the RN conditions. Two illumination angles $\psi = 0°$ (top panels) and $\psi = 60°$ (bottom panels) are considered.

The diffusion coefficients for gas–grain interaction (including neutral, ion, and plasma drag) are independent of the grain orientation and its angular momentum, whereas the diffusion coefficients for IR emission depend on $\mathbf{J}$. Hence, we can write

$$A_i' = \sum_{j=n,\mathrm{ion},p} A_j' + \langle A_{\mathrm{IR},i}'\rangle(J, \xi, \psi), \tag{28}$$

$$B_{ij}' = \sum_{j=n,\mathrm{ion},p} B_{ij,j}' + \langle B_{\mathrm{IR},ij}'\rangle(J, \xi, \psi), \tag{29}$$

where $\langle A_{\mathrm{IR}}'\rangle(J, \xi, \psi)$ and $\langle B_{\mathrm{IR}}'\rangle(J, \xi, \psi)$ are tabulated in the preceding section.

To solve the Langevin Equation (24) numerically, we use the second-order integrator (Vanden-Eijnden & Ciccotti 2006). Thus, the angular momentum component $j_i \equiv J_i'$ at iterative step $n + 1$ is evaluated as follows:

$$j_{i;n+1} = j_{i;n} - \gamma_i j_{i;n}h + \sqrt{h}\,\sigma_{ii}\zeta_n - \gamma_i \mathcal{A}_{i;n} - \gamma_{\mathrm{ed}}\mathcal{B}_{i;n}, \tag{30}$$

where h is the time step, $\gamma_i = 1/\tau_{\mathrm{gas,eff}}' + \delta_m(1 - \delta_{zi})$, $\gamma_{\mathrm{ed}} = 2/(3\tau_{\mathrm{ed,eff}}')$, $\sigma_{ii} = \sqrt{B_{ii}'}$, and

$$\mathcal{A}_{i;n} = -\frac{h^2}{2}\gamma_i j_{i;n} + \sigma_{ii}h^{3/2}g(\zeta_n, \eta_n) - \gamma_{\mathrm{ed}}j_{i;n}^3\frac{h^2}{2},$$

$$\mathcal{B}_{i;n} = j_{i;n}^3 h - 3\gamma_i j_{i;n}^3\frac{h^2}{2} - \frac{3j_{i;n}^5 \gamma_{\mathrm{ed}}h^2}{2}$$
$$+ 3j_{i;n}^2\sigma_{ii}h^{3/2}g(\zeta_n, \eta_n), \tag{31}$$

with η_n and ζ_n being independent Gaussian variables with zero mean and unit variance and $g(\zeta_n, \eta_n) = (\zeta_n + \eta_n/\sqrt{3})/2$ (see Hoang & Lazarian 2016a, for details).

The time step h is chosen by $h = 0.01$ minutes$[1/F_{\mathrm{tot},\parallel}, 1/G_{\mathrm{tot},\parallel}, \tau_{\mathrm{ed},\parallel}/\tau_{\mathrm{H},\parallel}, 1/\delta_m]$. As usual, the initial grain angular momentum is assumed to have random orientation in the space and magnitude $J = I_\parallel \omega_T$ (i.e., $j = 1$).

5. Parameter Space Study for PAH Alignment

5.1. Definition of Alignment Degree

Let $Q_X = \langle G_X\rangle$ with $G_X = (3\cos^2\theta - 1)/2$ be the degree of internal alignment of the grain symmetry axis $\hat{a}_1$ with $\mathbf{J}$, and let $Q_J = \langle G_J\rangle$ with $G_J = (3\cos^2\xi - 1)/2$ be the degree of external alignment of $\mathbf{J}$ with $\mathbf{B}$. Here the angle brackets denote the average over the ensemble of grains. The net degree of alignment of $\hat{a}_1$ with $\mathbf{B}$, namely, the Rayleigh reduction factor, is defined as $R = \langle G_X G_J\rangle$ (Greenberg 1968).

We calculate the degree of PAH alignment by solving the LEs. The LE is numerically solved for an integration time $T = 10^3 t_{\mathrm{gas}}$ and N steps, which ensures that T is much larger than the longest dynamical timescale to provide good statistical calculations of the degrees of grain alignment. The degree of alignment is then calculated by replacing the ensemble average with the time averaging as follows:

$$Q_J \equiv \sum_{n=1}^{N} \frac{G_J(\cos^2\xi_n)}{N}, \tag{32}$$

Table 1
Typical Parameters for the Idealized ISM Phases

Parameters	CNM	RN	PDR
n_H (cm^{-3})	30	10^3	10^5
T_{gas} (K)	100	100	1000
T_d (K)	20	40	80
U	1	1000	30000
$x_H \equiv n(H^+)/n_H$	0.0012	0.001	0.0001
$x_M \equiv n(M^+)/n_H$	0.0003	0.0002	0.0002
$y = 2n(H_2)/n_H$	0.0	0.5	0.5
B (μG)	10	100	100

$$Q_X = \frac{1}{N}\sum_{n=1}^{N}\frac{\bar{G}_X}{N}, \tag{33}$$

$$R = \sum_{n=1}^{N}\frac{G_J(\cos^2\xi_n)\bar{G}_X}{N}, \tag{34}$$

where $\bar{G}_X = \int_0^\pi G_X(\cos^2\theta)f_{LTE}(\theta, J_n)d\theta$.

The grain rotational temperature can be calculated as $T_{rot} = \langle J^2\rangle/k_B I_\parallel$, where $\langle J'^2\rangle = \sum_{i=1}^{N}J'^2/N$.

5.2. Numerical Results

5.2.1. Unidirectional Radiation Field

We first consider the conditions of RNe, where the illumination is unidirectional with anisotropy degree $\gamma_{rad} = 1$. We perform calculations by varying four parameters: the hydrogen ionization fraction x_H, the magnetic field B, the radiation intensity U, and the illumination direction ψ. For each varying parameter, the rest of the physical parameters are assumed to be the typical values of RNe, as shown in Table 1.

Figure 4 shows the degrees of alignment, Q_X, Q_J, R, and $\langle J'^2\rangle^{1/2}$, for the various illumination angles ψ, for $B = 50$ μG (left panel), 100 μG (middle panel), and 200 μG (right panel).

The degree of internal alignment Q_X and $\langle J'^2\rangle^{1/2}$ do not change significantly with ψ, whereas Q_J and R of the smallest PAHs ($a < 20$ Å) tend to increase with increasing ψ.[6] This is expected because for $\psi = 0°$ the maximum cross section of PAH absorption corresponds to the PAH plane perpendicular to the magnetic field. Thus, this realization induces strongest damping and randomization of PAH orientation, reducing the degree of alignment. When the magnetic field increases, the degree of external alignment increases thanks to stronger magnetic relaxation, but the increase in alignment degree with ψ is reduced.

Figure 5 shows the results for the higher ionization fraction $x_H = 0.005$ (top panels) and 0.01 (bottom panels). For the same magnetic field strength, we see the increase of $\langle J'^2\rangle^{1/2}$ and then the degrees of alignment with increasing x_H, which originates from ion collisions.

To see the dependence of alignment degree on the radiation intensity, we show in Figure 6 the alignment degree for two different radiation fields. The stronger radiation field results in a much lower degree of alignment due to more efficient

---

damping by IR emission (see the right panel). However, the effect of anisotropic illumination is much stronger for this case, leading to a significant increase of Q_J and R with ψ for small PAHs below 10 Å.

We note the negligible dependence of rotational temperature on the illumination direction ψ. This reveals that the enhanced alignment with ψ is mainly due to the differential cross section, not paramagnetic relaxation.

5.2.2. The Diffuse ISM: CNM

For completeness, Figure 7 shows the results for the diffuse ISM (CNM) with the typical anisotropy degree of radiation $\gamma = 0.1$. A sharp rise at $a \sim 4.5$Å is a numerical artifact, which is well below the numerical accuracy achieved by LE simulations (see Roberge & Lazarian 1999). The dependence of PAH alignment on the illumination angle is negligible, as expected from the low degree of anisotropy.

6. Polarization of Spinning Dust Emission

6.1. Spinning Dust Model

We calculate the spinning dust emissivity and polarized emissivity per H as

$$\frac{j_{\nu,em}}{n_H} = \int_{a_{min}}^{a_{max}} j_\nu(a)\frac{dn}{n_H da}da, \tag{35}$$

$$\frac{j_{\nu,pol}}{n_H} = \int_{a_{min}}^{a_{max}} Q_J(a)\cos^2\gamma_B j_\nu(a)\frac{dn}{n_H da}da, \tag{36}$$

where $j_\nu(a)$ is the emissivity by a grain of size a, Q_J is the degree of external alignment, and γ_B is the angle between $\boldsymbol{B}$ and the plane of the sky, which is assumed to be $\gamma_B = 0$ in the following calculations. Here $a_{min} = 3.5$ Å and $a_{max} = 100$ Å are the lower and upper cutoffs, respectively, of the PAH size distribution dn/da. We use the advanced spinning dust model in Hoang et al. (2011) to calculate $j_\nu(a)$. Here we adopt the PAH size distribution dn/da from Weingartner & Draine (2001), with the C abundance contained in PAHs of $b_C = 6 \times 10^{-5}$.

### 6.2. Emission and Polarization Spectrum

6.2.1. Unidirectional Radiation: RNe

In the top panels of Figure 8, we present the total spinning emissivity and polarized emissivity from PAHs in the RNe, computed for the different illumination angles ψ and ionization fraction $x_H = 0.005$. The left panel shows the results for $B = 50$ μG, the middle panel for $B = 100$ μG, and the right panel for $B = 200$ μG. A slight decrease of the emissivity is found when the field strength is increased, which is a direct consequence of the fast dissipation of rotational energy into heat via magnetic relaxation.

The bottom panels show the polarization degree versus the frequency. The polarization increases with the frequency and reaches a nearly saturated value between $p \sim 10\%$ and 20% at $\nu > 70$ GHz for $B \geqslant 100$ μG (middle and right panels). The transition frequency of the polarization essentially coincides with the peak frequency of the emissivity, which can facilitate observations. For a given magnetic field, the polarization increases

---

[6] Note that the numerical error in R obtained with the Langevin simulations is $\sim$0.001 (Roberge & Lazarian 1999; Hoang et al. 2014); thus, we are not discussing the results for $a > 20$ Å.
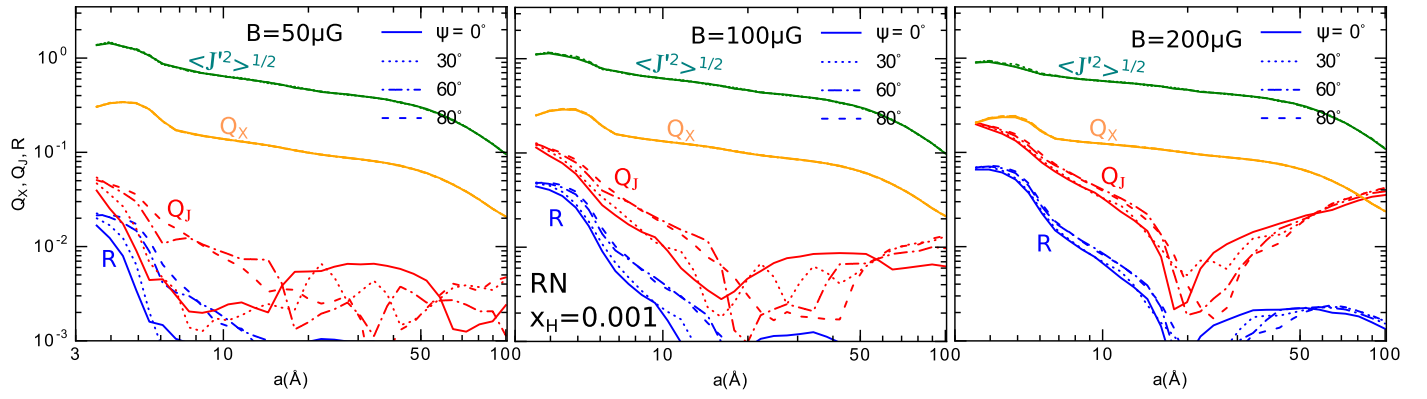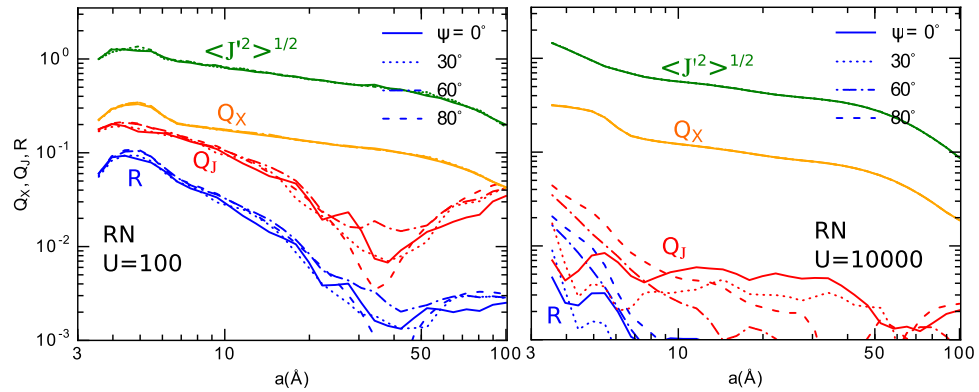
Figure 4. Degrees of PAH alignment in the RN conditions vs. the grain size for the different illumination angles (ψ) and the hydrogen ionization fraction $x_H = 0.001$. Left, middle, and right panels show the results for $B = 50$, 100, and 200 μG, respectively.
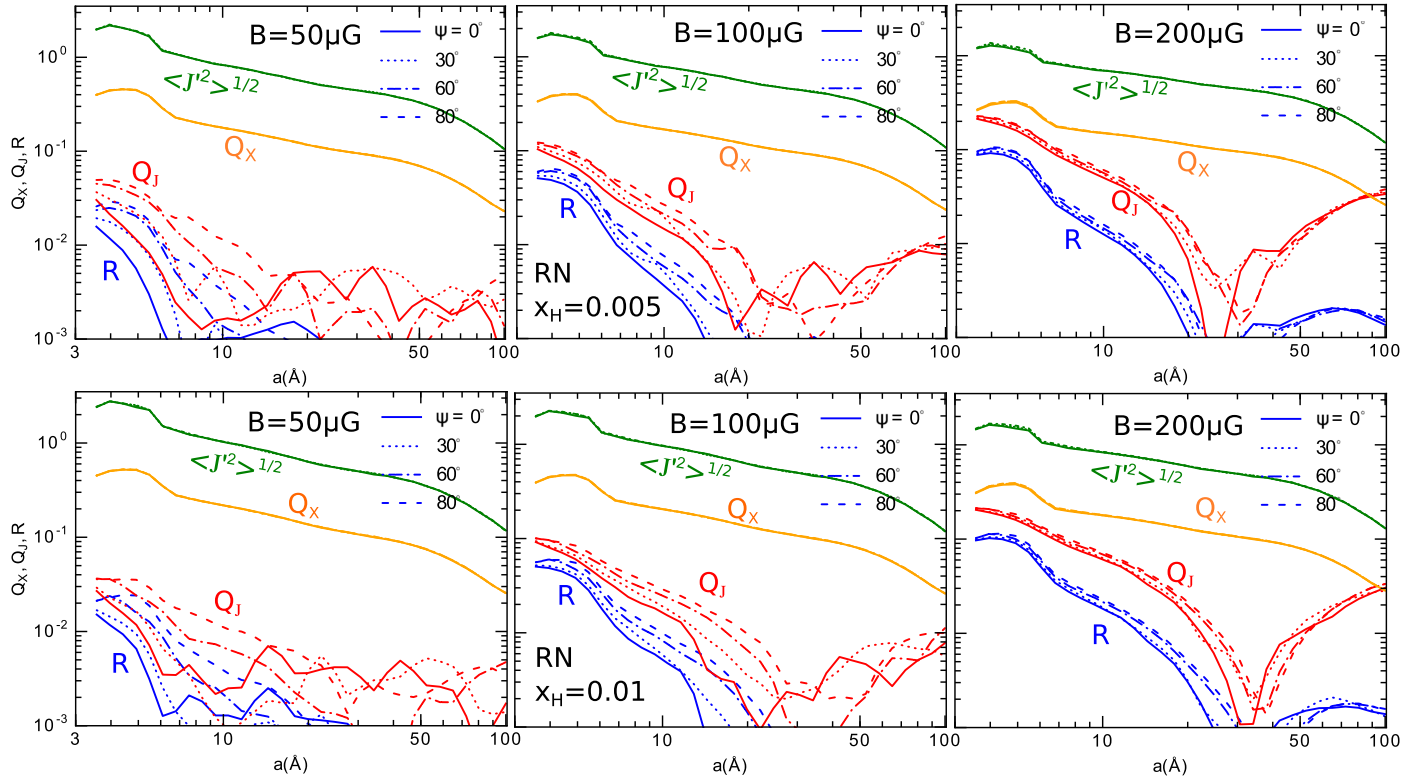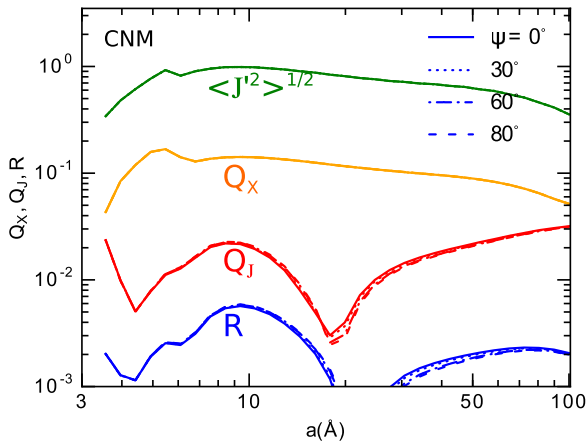

Figure 5. Same as Figure 4, but for $x_H = 0.005$ (top panels) and 0.01 (bottom panels).

Figure 6. Same as Figure 4, but for a weak radiation field ($U = 10^2$) and very strong radiation field ($U = 10^4$).

Figure 7. Degrees of PAH alignment in the CNM with an anisotropy degree $\gamma = 0.1$ and $B = 10\,\mu$G.

with the illumination angle ψ, but the level of such an increase is reduced when the magnetic field is increased. For instance, at $\nu \sim 100$ GHz, the polarization ratio $p(\psi = 80°)/p(\psi = 0°) \sim 1.6$ for $B = 50\,\mu$G, and it reduces to $p(\psi = 80°)/p(\psi = 0°) \sim 1.05$ for $B = 200\,\mu$G (see Figure 8).

Same as Figure 8, but Figures 9 and 10 show the results for two cases, with lower and higher ionization fractions $x_H = 0.001$ and $x_H = 0.01$, respectively. The emissivity is found to vary with x_H owing to weaker/stronger ion excitation, as expected. The polarization degree increases with ψ, in a similar trend to that seen in Figure 8 (bottom panels).

The top panels of Figure 11 show the total and polarized spinning dust emissivity for three cases of $U = 10^2$, 10^3, and $U = 10^4$, corresponding to a weak, typical, and a strong radiation field. We also plot the results for thermal dust, both total emission and polarized emission, assuming a fixed polarization fraction of 20% (see Appendix B). Spinning dust dominates over thermal dust for $\nu < 150$ GHz, whereas polarized spinning dust dominates at $\nu < 100$ GHz.

The bottom panels of Figure 11 show the polarization degree from spinning dust, thermal dust, and the total polarization by thermal dust plus spinning dust (solid lines). The polarization degree of spinning dust emission tends to decrease with increasing U, which arises from the fact that the stronger radiation induces faster rotational damping by IR emission and thus the lower degree of alignment. However, the increase of the polarization with ψ is much larger, e.g., $p(\psi = 80°)/p(\psi = 0°) \sim 2$ at $\nu \geqslant 100$ GHz (see the right panel). The total polarization by thermal dust and spinning dust is dominated by thermal dust polarization at $\nu > 100$ GHz and by spinning dust at $\nu < 60$ GHz (see solid lines).

6.2.2. Unidirectional Radiation: PDRs

Figure 12 shows spinning dust emissivity (top panels) and polarization spectrum (bottom panels) computed for the different ψ and $x_H = 10^{-4}$, 10^{-3}, 10^{-2} for the PDR conditions. Thermal dust emission and polarized thermal dust emission are also shown in black dashed and dotted lines, respectively. Spinning dust dominates over thermal dust at frequencies $\nu < 300$ GHz.

As shown in Figure 12 (bottom panels), the polarization of spinning dust can only reach $p \sim 2\%$ for $\nu > 20$ GHz. This polarization level is much lower than in RNe (see Figures 8–11) because the PDR conditions have much higher IR damping, for which PAHs are rotating subthermally and less efficiently aligned

according to the magnetic relaxation mechanism (Hoang 2017). Yet the increase in the polarization with ψ is much more pronounced.[7]

The influence of polarized spinning dust emission results in the change in the polarization spectrum at $\nu < 200$ GHz. Indeed, the polarization degree is decreasing with decreasing ν rather than being flat if only thermal dust emission is considered.

We note that the present results are obtained assuming the existence of small PAHs in PDRs, with $a_{min} = 3.5$ Å and the peak size of PAH mass distribution $a_p \sim 6$ Å. Such small PAHs are expected to be destroyed by photodissociation in the PDR conditions, leading to an increase in a_p with the stellar temperature and luminosity (see Seok & Li 2017). As a result, spinning dust emissivity in realistic PDRs is likely lower than shown in Figure 12 (see Hoang et al. 2011).

6.2.3. The Diffuse CNM

For sake of completeness, in Figure 13 we show the results for the CNM with the low anisotropy degree of $\chi = 0.1$. Both emissivity and polarization show a negligible increase with increasing ψ. The degree of polarization is low, peaks at $\nu \sim 3$ GHz, and becomes smaller than 1.5% for $\nu > 20$ GHz.

The spinning dust is dominant over thermal dust at $\nu < 70$ GHz. The polarized spinning dust can slightly increase the total polarized emission from thermal dust.

7. Discussion

7.1. Alignment of PAHs in an Anisotropic Radiation Field: Magnetic Relaxation versus Cross Section

Resonance paramagnetic relaxation was first suggested by Lazarian & Draine (2000) as a way to align PAHs and paramagnetic nanoparticles. Later, numerical calculations in Hoang et al. (2014) found that resonance relaxation can enable PAHs to be aligned up to a degree of ~10% (see also Hoang 2017). These studies assumed that PAHs are illuminated by the isotropic diffuse interstellar radiation and disregard the effect of the anisotropic radiation field.

Lazarian (1995a) suggested a cross-sectional mechanism for aligning classical grains subject to a gas flow. The essence of the mechanism is that the rate of the diffusion of the grain angular momentum can change depending on the cross section that the planar grain exposes to the flow of atoms, resulting in the alignment of grains that minimizes its cross section. The cross-sectional alignment for classical grains requires the directed flow of hydrogen atoms, which may be difficult to get for ultrasmall grains, which usually move with relatively small velocities with respect to the gas. However, the differences in cross sections (see Section 3) are important for the radiation that interacts with PAHs. This induces a similar effect that the grain stays statistically longer in the position of its minimal cross section.[8]

---

[7] The polarization below ~0.5% is within the numerical errors of the Langevin simulations, such that the angle dependence is not discussed.

[8] Other mechanical processes of alignment, e.g., Gold alignment (Gold 1952; Dolginov & Mitrofanov 1976; Lazarian 1994), also formally make the cross section of the grain interaction with the flow minimal. However, this is done through the depositing of the angular momentum with the grain. The cross-sectional mechanism is based on different physics. It is based on the dependence of the diffusion of the angular momentum on the grain-flow cross section. In Lazarian (1995b) this was due to the changing rate of crossovers depending on the cross section; in the present paper this is due to the change of the rate of the photon emission depending on grain-radiation cross section.
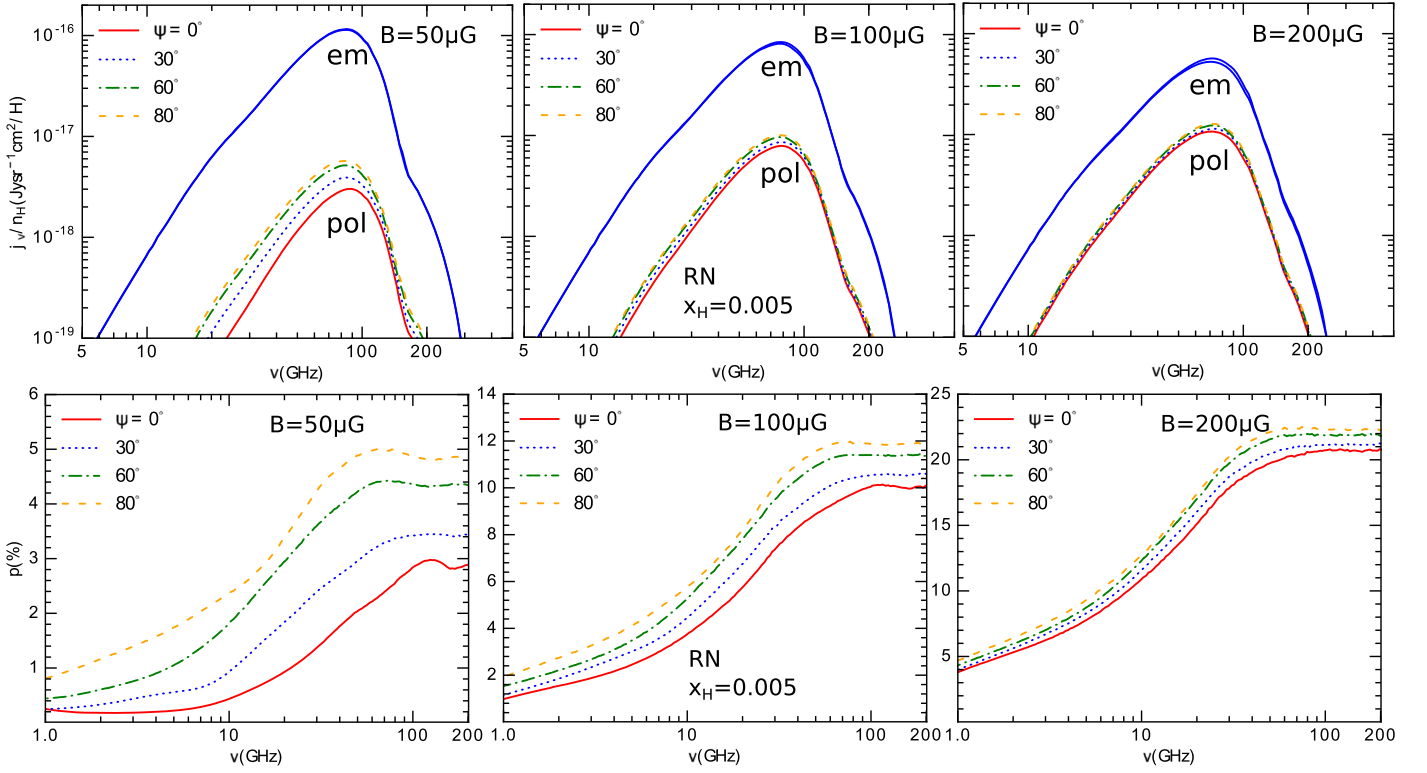
Figure 8. Top panels: unpolarized and polarized spinning dust emissivity by spinning PAHs in RNe with $x_H = 0.005$ and $U = 1000$, computed for the different illumination directions ψ. Bottom panels: frequency-dependence polarization degree of spinning dust emission. Three values of the magnetic field strength, $B = 50~\mu G$ (left panel), $100~\mu G$ (middle panel), and $200~\mu G$ (right panel), are considered.
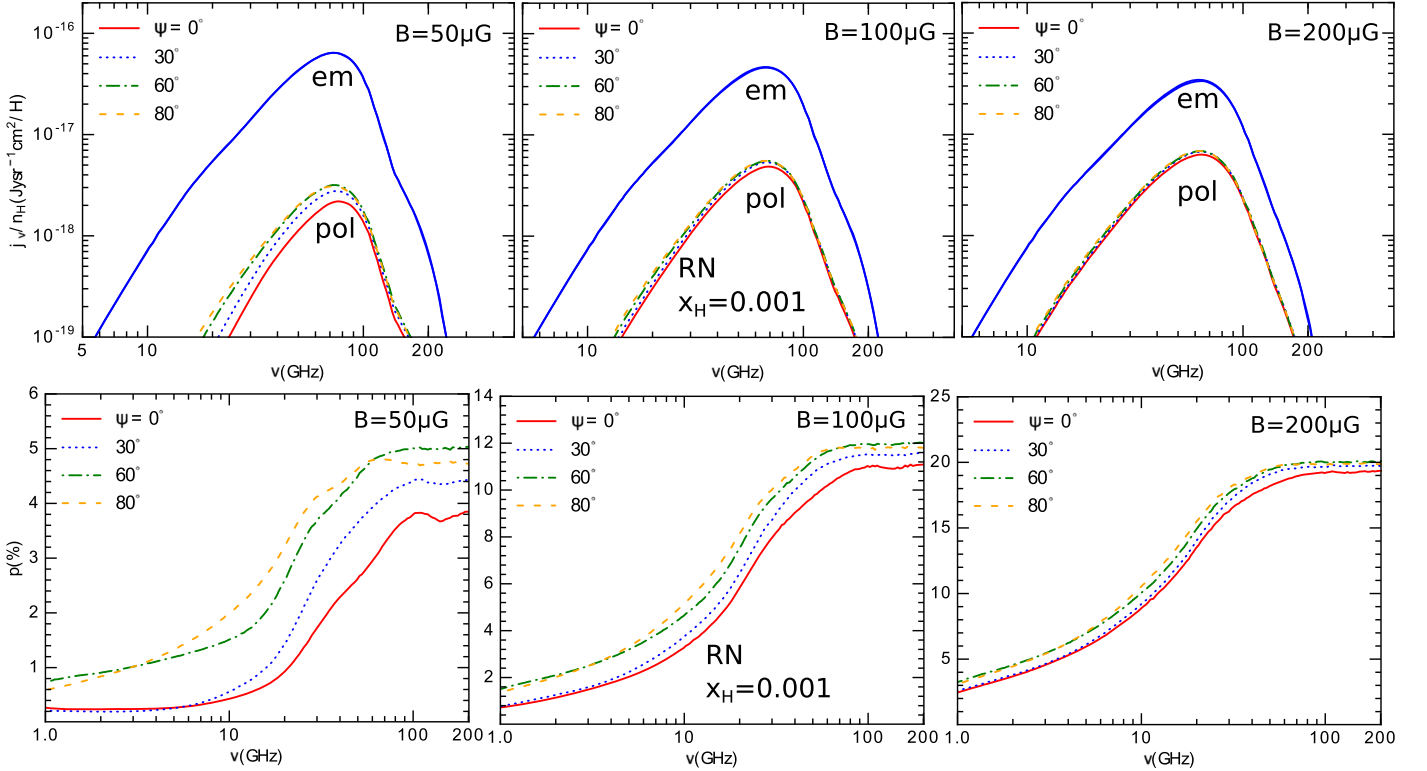

**Figure 9.** Similar to Figure 8, but for $x_H = 0.001$.

In this paper, we simultaneously treat PAH alignment by paramagnetic relaxation and cross-sectional mechanism in the presence of anisotropic radiation fields. To identify the efficiency of both mechanisms, we perform calculations for the different magnetic field strengths and illumination directions. We have quantified the alignment of PAHs in three
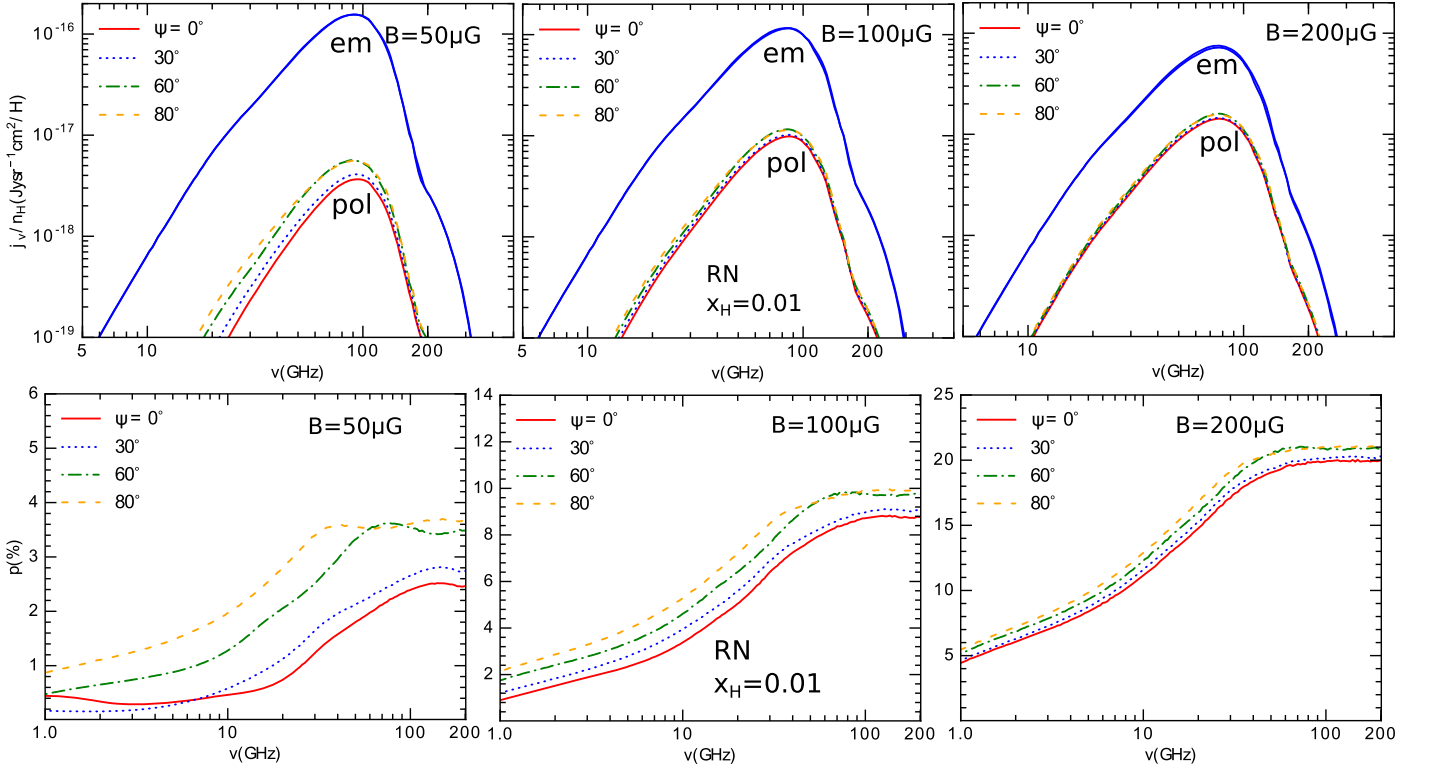
Figure 10. Similar to Figure 8, but for $x_H = 0.01$.
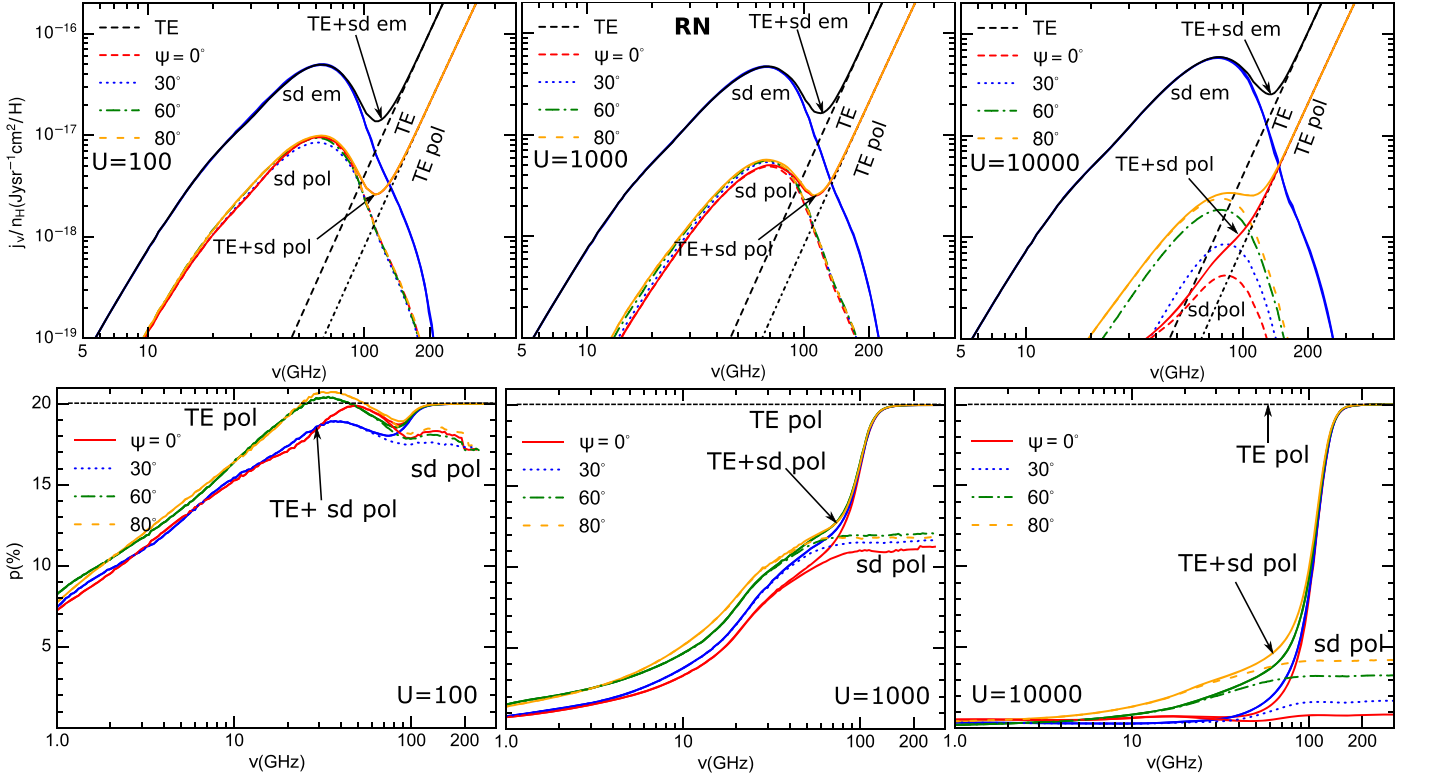
Figure 11. Spinning dust emissivity (top panels) and polarization fraction (bottom panels) for RNe with different radiation strengths: $U = 10^2$, 10^3, and $U = 10^4$. Thermal emission intensity and polarization are also shown in black dashed and dotted lines. The increase of the polarization degree of spinning dust with ψ is more pronounced for $U = 10^4$.
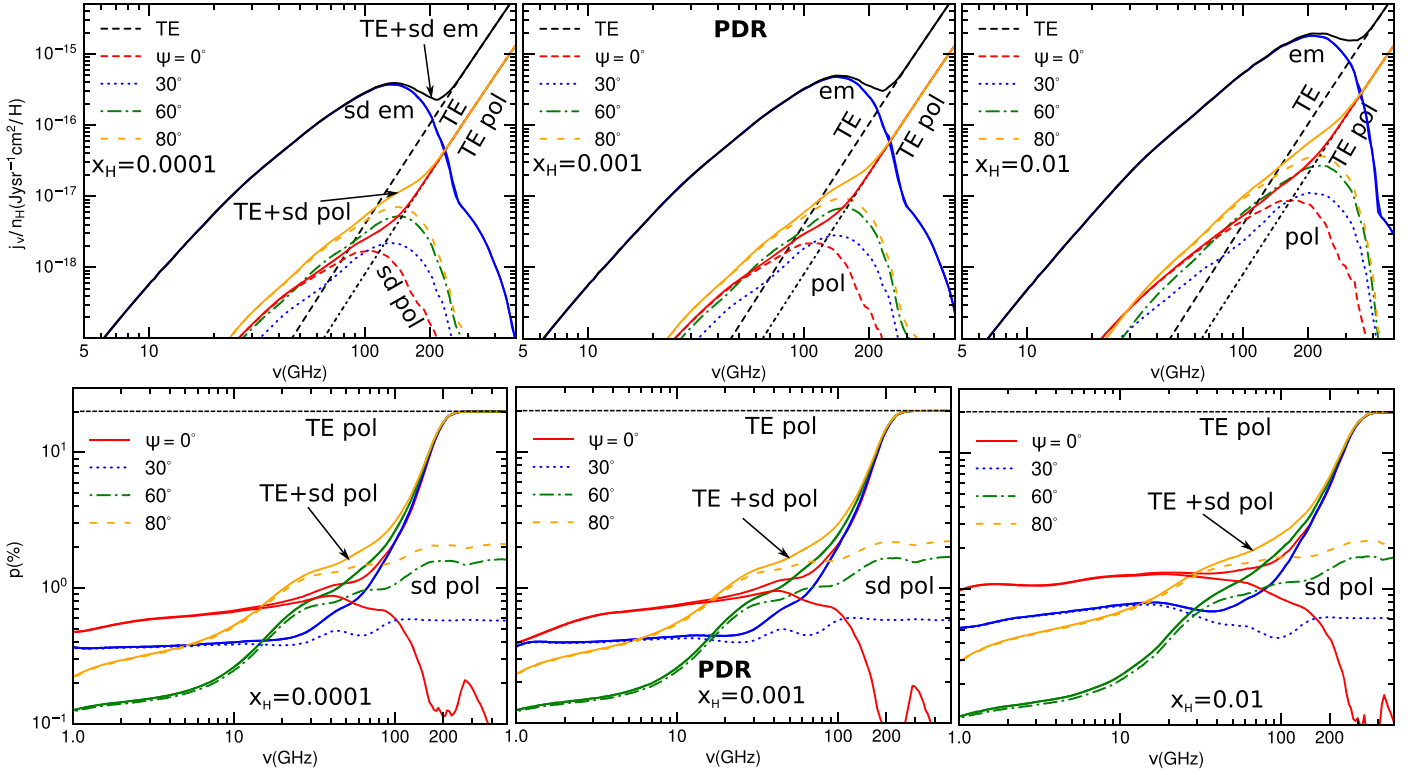
Figure 12. Same as Figure 11, but for the standard PDR with varying ionization fraction x_H. Thermal emission intensity and polarization are also shown in black dashed and dotted lines, respectively.
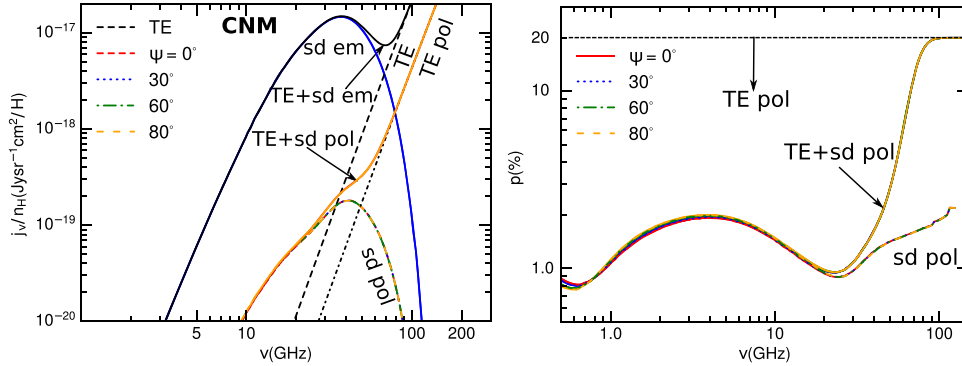
Figure 13. Spinning dust emissivity (left panel) and polarization spectrum (right panel) for the CNM with a degree of anisotropy of $\gamma = 0.1$.

environment conditions, RNe, PDRs, and CNM, with various physical parameters. For the unidirectional radiation fields (RNe and PDRs with anisotropy degree $\gamma = 1$), we demonstrate that the anisotropic radiation can increase the degree of PAH alignment, with the alignment degree increasing with the angle between the radiation direction and the magnetic field. This is expected from the cross-sectional mechanism acting on the photon–grain interaction. The cross-sectional process is more efficient when the magnetic field is lower; thus, one may estimate the efficiency of the cross-sectional mechanism based on the alignment efficiency obtained for a very weak magnetic field. In this sense, we found that the alignment efficiency Q_J cannot exceed 5% for $B = 50\,\mu G$ in the RN conditions (see the right panels in Figures 4 and 5).

Moreover, among the considered environments, we found that PAHs are more efficiently aligned in the RN conditions, where the gas density is not as high as in PDRs, which originates from the resonance paramagnetic relaxation

mechanism. A low degree of PAH alignment in the CNM (i.e., $\gamma = 0.1$) obtained in this study is consistent with our previous studies where isotropic radiation field is assumed (Hoang et al. 2014).

7.2. Polarization of Spinning PAH Emission and Comparison with Observations

Using the obtained degree of PAH alignment, we calculate spinning dust emissivity, both total emission and polarized emission. For the diffuse ISM (i.e., CNM), we find that the polarization of spinning PAH emission is about 2% peak at 5 GHz and declines rapidly to below 1% at $\nu > 20$ GHz.

For the RN conditions, we find that the polarization degree can be large, increasing from 5% at 10 GHz to 20% at 100 GHz. The peak polarization is close to the peak of emission intensity, which favors the detection of the polarization. The difference arises from the fact that in the RNe the degree of

alignment increases with the PAH size for $a < 10$ Å, whereas the alignment decreases rapidly for the CNM (see Figures 4 and 7). Such a difference arises from the excitation by ion collisions that dominates the rotational excitation in the RNe for the smallest PAHs with negative charges. The effect of cross-sectional mechanism is particularly important for the RN and PDR conditions. We find that for the RNe the polarization degree can be increased by 200% when the illumination direction is changed from parallel to nearly perpendicular to the magnetic field. In the PDR, the polarization is lower because of the dominant damping and randomization by gas collisions, but the efficiency of the cross-sectional mechanism is stronger (see Section 6).

The theoretical predictions for the polarization of spinning PAH emission in the CNM appear to be consistent with the available observational data. For instance, several observational studies (Battistelli et al. 2006, 2015; Mason et al. 2009; Dickinson et al. 2011) have found the upper limits for the AME polarization to be between 1% and 5%. An upper limit of 1% is also reported in various studies (see López-Caraballo et al. 2011; Rubiño-Martín et al. 2012; Génova-Santos et al. 2017). The latest results by Planck Collaboration et al. (2015a) show the AME polarization to be 0.6% ± 0.5%, consistent with our calculations for the CNM. Observations for the polarization of AME from RNe are not yet available. Nevertheless, in the light of this study, we suggest that future observations for the polarization of AME should search for polarized spinning dust emission in the RN conditions. Note that our theoretical results are obtained assuming that the magnetic field is perpendicular to the line of sight. It is known that the ISM is magnetized and turbulent. As a result, the magnetic field wandering can reduce the polarization degree presented in this paper.

7.3. Implications for Polarized Infrared Emission and Tracing Magnetic Fields

If PAHs are indeed aligned with the magnetic fields, then we can probe the magnetic fields in the RN conditions, such as circumstellar disks around T Tauri and Herbig Ae/Be stars via mid-IR polarization (Hoang 2017). Moreover, expecting the same alignment of nanosilicates by resonance relaxation, the polarization of the $\sim 10\ \mu$m silicate emission feature is perhaps comparable to that of the 11.3 μm feature. RAT alignment theory predicts that very large grains are not aligned with respect to the magnetic field because the Larmor precession becomes slower than gas randomization (see Equation (41) in Hoang & Lazarian 2016b). Instead, these very large grains are predicted to be aligned with respect to the anisotropic radiation direction (Lazarian & Hoang 2007b). The incorporation of iron inclusions in dust grains can enhance the maximum size of grains that are still coupled to the magnetic field (Hoang & Lazarian 2016b). Such a maximum size as a function of the local gas density, magnetic field strength, and iron inclusions can be estimated using Equation (42) in Hoang & Lazarian (2016b). We note that the alignment along the radiation direction is first theoretically studied by Lazarian & Hoang (2007b) and is modeled by Tazaki et al. (2017) for protoplanetary disks. As a result, millimeter wavelength polarization may not be able to trace the magnetic field in circumstellar disks. ALMA observations of HL Tau at 3.1 mm by Kataoka et al. (2017) and at 1.3 mm by Stephens et al. (2017) show that the polarization patterns are azimuthal, as expected from the polarization produced by grains aligned with

the radiation direction (Tazaki et al. 2017). Thus, mid-IR polarization appears to be a useful way to trace magnetic fields in the surface layer of circumstellar disks, where grains are expected to be aligned with the magnetic field (see, e.g., Li et al. 2016).

7.4. Effect of Temperature Fluctuations on Nanoparticle Alignment in Intense Radiation Environments

In the present paper, to capture the effect of anisotropic illumination on PAH alignment, the temperature of PAHs is assumed to be fixed. In realistic conditions, the temperatures of small PAHs undergo strong fluctuations, with frequent thermal spikes after single-photon absorption (Guhathakurta & Draine 1989). Let us now discuss the effect of temperature fluctuations on PAH alignment.

For a typical PAH of size 10 Å, the mean time between two UV photon absorption events is $\tau_{abs} \sim (10^6/U)$ s, while the radiative cooling time via IR emission is $\tau_{rad} \sim 100$ s (Draine & Li 2001). In the RN and PDR conditions with $U \gtrsim 10^3$, one has $\tau_{rad} \gtrsim \tau_{abs}$, for which the PAH molecule cannot cool completely before a subsequent UV photon absorption. Therefore, the PAH temperature undergoes frequent fluctuations, but the amplitude of fluctuations is smaller than in the case of standard diffuse radiation field with $\tau_{rad} \ll \tau_{abs}$ (i.e., CNM). For PAHs smaller than 10 Å, the effect of thermal spikes is more important because the radiation time becomes much shorter than the absorption time (see Draine & Li 2001).

The magnetic alignment timescale by paramagnetic relaxation is $\tau_{mag} \sim 0.5(a/10\ \text{Å})^2(B/100\ \mu\text{G})^{-2}(1.2 \times 10^{-13}\ \text{s}/K(\omega))$ yr, where $K(\omega) = \chi_2/\omega$, with χ_2 the imaginary part of magnetic susceptibility (see Hoang & Lazarian 2016b). This timescale is much longer than the thermal spike timescale, as well as internal relaxation. Therefore, an adequate treatment of grain alignment needs to average the damping and diffusion coefficients over the grain temperature distribution (e.g., Draine & Hensley 2016). Such a study is beyond the scope of this paper, which is aimed at quantifying the effect of cross-sectional alignment only. Nevertheless, we expect temperature fluctuations to reduce the degree of internal alignment and external alignment because of stronger thermal fluctuations during the spikes. For instance, Hoang (2017) shows a significant decrease in the alignment degree with increasing grain temperature prior to UV photon absorption T_0.

8. Summary

We have quantified the cross-sectional mechanism of grain alignment that is based on the difference in the rate of the photon absorption by PAHs depending on its orientation relative to the photon flux and computed the polarization of microwave emission arising from rapidly spinning PAHs. Our principal results are summarized as follows:

1. We calculated the averaged diffusion coefficients by IR emission over the torque-free motion of PAHs, thermal fluctuations, and fast Larmor precession. We demonstrated that the averaged coefficients exhibit anisotropy for suprathermal rotation but are nearly isotropic for subthermal rotation.

2. We numerically computed the degree of PAH alignment by varying the illumination angle ψ relative to the magnetic field. For the unidirectional radiation fields of RNe and PDRs, we find that the degree of alignment tends to increase with increasing ψ. For the diffuse ISM

13

(CNM), the variation of alignment with ψ is negligible owing to a low degree of anisotropy. The alignment of PAHs in the RN conditions is the most efficient compared to that in the CNM and PDR.

3. Our numerical results demonstrate that the cross-sectional alignment can also work for photon–grain interactions in an anisotropic radiation field, but the resulting alignment efficiency is moderate. The resonance paramagnetic relaxation still plays a dominant role in aligning PAHs with the magnetic field. The obtained degree of PAH alignment can successfully explain the polarization of 2% observed at 11.3 μm from the MWC 1080 nebula by Zhang et al. (2017), as shown in Hoang (2017).

4. We predicted the polarization degree of spinning PAH emission in the RNe, PDRs, and CNM. We found that the polarization degree is low for the diffuse regions (CNM) and PDRs, but can be large, up to 20%, for the RN conditions and tends to increase with the illumination direction. The peak polarization is close to the peak emission, which reveals that RNe are the most favored conditions for detecting the spinning dust polarization.

Appendix A
Coordinate Systems and Transformation

A.1. Definitions of Coordinate Systems

Assume that a PAH is illuminated by radiation from a nearby star with the propagation vector $\hat{k}$.

To account for an external source such as a star, we introduce a frame of reference $\hat{x}_k \hat{y}_k \hat{z}_k$, where $\hat{z}_k$ is directed along the radiation direction $\boldsymbol{k}$.

Let $\hat{\boldsymbol{a}}_1$, $\hat{\boldsymbol{a}}_2$, $\hat{\boldsymbol{a}}_3$ be the grain principal axes, where $\hat{\boldsymbol{a}}_1$ is the axis of maximum moment of inertia. For the axisymmetric shape of PAHs, $\hat{\boldsymbol{a}}_2$ is chosen along the line of node (see Figure 2).

Let $\hat{x}_J \hat{y}_J \hat{z}_J$ are unit vectors in which $\hat{z}_J$ is parallel to $\boldsymbol{J}$, $\hat{x}_J$ is directed along $\hat{\xi}$, and $\hat{y}_J$ is directed along $\hat{\phi}$ (see Figure 2). Let $\hat{x}_B \hat{y}_B \hat{z}_B$ be unit vectors defined by the magnetic field in which $\hat{z}_B \| \boldsymbol{B}$. The orientation of $\boldsymbol{J}$ in the B-frame is determined by two angles ξ and ϕ.

A.2. Transformation of Coordinate Systems

The alignment of $\boldsymbol{J}$ with respect to the magnetic field is determined by the angles ξ, ϕ in the magnetic field coordinate system. The transformation from vector basis $\hat{\boldsymbol{e}}$ to a new basis $\hat{\boldsymbol{e}}'$ is done through matrix transformation:

$$\hat{\boldsymbol{e}}_i = T_{ij} \hat{\boldsymbol{e}}_j, \tag{37}$$

where T is the transformation matrix from reference frame $\hat{\boldsymbol{e}}$ to $\hat{\boldsymbol{e}}'$.

For an axisymmetric grain with the angles defined in Figure 2, we have the following (see Appendix A in Hoang

et al. 2011):

$$\hat{\boldsymbol{a}}_1 = \cos\theta \hat{z}_J + \sin\theta (\sin\zeta \hat{x}_J - \cos\zeta \hat{y}_J), \tag{38}$$

$$\hat{\boldsymbol{a}}_2 = \cos\zeta \hat{x}_J + \sin\zeta \hat{y}_J, \tag{39}$$

$$\hat{\boldsymbol{a}}_3 = [\hat{\boldsymbol{a}}_1 \times \hat{\boldsymbol{a}}_2] = \sin\theta \hat{z}_J + \cos\theta (-\sin\zeta \hat{x}_J + \cos\zeta \hat{y}_J), \tag{40}$$

where ζ denotes the rotation angle around $\hat{\boldsymbol{a}}_1$, e.g., the line of node N can be chosen to be along $\hat{\boldsymbol{a}}_2$.

From $\boldsymbol{J}$-frame to $\boldsymbol{B}$-frame, we get

$$\hat{z}_J = \cos\xi \hat{z}_B + \sin\xi (\cos\phi \hat{x}_B + \sin\phi \hat{y}_B), \tag{41}$$

$$\hat{x}_J = -\sin\xi \hat{z}_B + \cos\xi (\cos\phi \hat{x}_B + \sin\phi \hat{y}_B), \tag{42}$$

$$\hat{y}_J = [\hat{z}_J \times \hat{x}_J] = \cos\phi \hat{y}_B - \sin\phi \hat{x}_B, \tag{43}$$

where $\hat{y}_J$ lies in the $\hat{x}_B \hat{y}_B$ plane.

The direction of $\boldsymbol{B}$ in k-frame is determined by the angle ψ and ζ to consider for the 3D magnetic field. The transformation from B-frame to k-frame is given by

$$\hat{z}_B = \cos\psi \hat{z}_k + \sin\psi (\cos\zeta \hat{x}_k + \sin\zeta \hat{y}_k), \tag{44}$$

$$\hat{x}_B = -\sin\psi \hat{z}_k + \cos\psi (\cos\zeta \hat{x}_k + \sin\zeta \hat{y}_k), \tag{45}$$

$$\hat{y}_B = [\hat{z}_B \times \hat{x}_B] = \cos\zeta \hat{y}_k - \sin\zeta \hat{x}_k. \tag{46}$$

It follows that

$$\cos\beta = \hat{z}_J.\hat{z}_k = \cos\xi \cos\psi - \sin\xi \cos\phi \sin\psi, \tag{47}$$

$$\sin\beta \cos\varphi = \hat{z}_J.\hat{x}_k = \cos\xi \sin\psi \cos\zeta$$
$$+ \sin\xi (\cos\phi \cos\psi \cos\zeta - \sin\phi \sin\zeta). \tag{48}$$

Let ψ be the angle between $\hat{z}_k$ and $\hat{z}_B$. Then, the angle Θ between $\hat{\boldsymbol{a}}_1$ and k ($\hat{z}_k$) is given by

$$\cos\Theta = \hat{\boldsymbol{a}}_1.\hat{z}_k = \cos\theta \hat{z}_J.\hat{z}_k + \sin\theta (\sin\zeta \hat{x}_J.\hat{z}_k - \cos\zeta \hat{y}_J.\hat{z}_k). \tag{49}$$

From Equations (41)–(46), we obtain

$$\hat{z}_J.\hat{z}_k = \cos\xi \cos\phi - \sin\xi \cos\phi \sin\psi, \tag{50}$$

$$\hat{x}_J.\hat{z}_k = -\sin\xi \cos\phi - \cos\xi \cos\phi \sin\psi, \tag{51}$$

$$\hat{y}_J.\hat{z}_k = \sin\phi \sin\psi. \tag{52}$$

A.3. Transformation of the Diffusion Coefficients

Note that the final diffusion coefficients in the lab system are already presented in Hoang et al. (2010). Here we present the derivation of these coefficients by following the transformation of the damping and diffusion coefficients from the grain-body frame to the lab frame defined by the magnetic field.

A.3.1. Body System to J-frame and Averaging over the Grain Precession

Let us consider the transformation of the diffusion coefficients from the body frame to the $\boldsymbol{J}$-frame. In the body frame, the damping coefficients for an axisymmetric grain (oblate) are described as

$$A_z^b \equiv \left\langle \frac{\Delta J_z^b}{\Delta t} \right\rangle = -\frac{J_z^b}{\tau_1}, \tag{53}$$

$$A_{x,y}^b \equiv \left\langle \frac{\Delta J_{x,y}^b}{\Delta t} \right\rangle = -\frac{J_{x,y}^b}{\tau_2}, \tag{54}$$

where $\tau_1 = \tau_\parallel$, $\tau_2 = \tau_\perp$ denote the characteristic damping timescale for the rotation along the grain symmetry and perpendicular axis, respectively.

The increment of $\boldsymbol{J}$ after a time interval Δt is evaluated in the body frame as $\Delta \boldsymbol{J}^b$. For the body frame defined with $\hat{\boldsymbol{a}}_2$ along the line of node, the vector $\Delta \boldsymbol{J}^b$ can be transformed to the $\boldsymbol{J}$-frame as follows:

$$\Delta J_z = \Delta J_z^b \cos\theta + \Delta J_y^b \sin\theta, \tag{55}$$

$$\Delta J_x = \Delta J_x^b \cos\phi - \Delta J_y^b \cos\theta \sin\phi + \Delta J_z^b \sin\theta \sin\phi, \tag{56}$$

$$\Delta J_y = \Delta J_x^b \sin\phi + \Delta J_y^b \cos\theta \cos\phi - \Delta J_z^b \sin\theta \sin\phi. \tag{57}$$

Averaging over the precession angle ϕ of the grain around $\hat{\boldsymbol{a}}_1$, we obtain

$$A_{x,y}^J \equiv \left\langle \frac{\Delta J_{x,y}}{\Delta t} \right\rangle = 0, \tag{58}$$

$$A_z^J \equiv \left\langle \frac{\Delta J_z}{\Delta t} \right\rangle = \left\langle \frac{\Delta J_z^b}{\Delta t} \right\rangle \cos\theta + \left\langle \frac{\Delta J_z^b}{\Delta t} \right\rangle \sin\theta$$

$$= -\frac{J_z^b}{\tau_1} \cos\theta - \frac{J_y^b}{\tau_2} \sin\theta. \tag{59}$$

With the choice of $\boldsymbol{J}$ so that the $\boldsymbol{J}$ is directed along $\hat{z}$, we have $\boldsymbol{J} = J_z^b \hat{z}_b + J_y^b \hat{y}_b$, $J_z^b = J_z \cos\theta$, and $\tan\theta = J_y^b / J_z^b$. Therefore, we obtain

$$\left\langle \frac{\Delta J_z}{\Delta t} \right\rangle = -\frac{J_z^b}{\tau_1} \left(\cos\theta + \frac{\tau_1}{\tau_2} \sin\theta \tan\theta \right)$$

$$= \left\langle \frac{\Delta J_z^b}{\Delta t} \right\rangle \left(\cos\theta + \frac{\tau_1}{\tau_2} \sin\theta \tan\theta \right) \tag{60}$$

$$= -\frac{J_z^b}{\cos\theta\,\tau_1} \left(\cos^2\theta + \frac{\tau_1}{\tau_2} \sin^2\theta \right)$$

$$= -\frac{J_z}{\tau_1} \left(\cos^2\theta + \frac{\tau_1}{\tau_2} \sin^2\theta \right) = -\frac{J_z}{\tau_{\rm eff}}, \tag{61}$$

where

$$\tau_{\rm eff} = \tau_1 \epsilon(\theta), \quad \epsilon(\theta) = \frac{1}{\cos^2\theta + \gamma \sin^2\theta}, \quad \gamma = \frac{\tau_1}{\tau_2}. \tag{62}$$

The above equation corresponds to the transformation of the damping coefficient:

$$A_z^J = A_z^b \frac{\left(\cos^2\theta + \frac{\tau_1}{\tau_2} \sin^2\theta \right)}{\cos\theta}. \tag{63}$$

Similarly, after averaging the diffusion coefficients over the grain precession, we obtain the diffusion coefficients in the $\boldsymbol{J}$-system:

$$B_{xx}^J \equiv \left\langle \frac{(\Delta J_{xx})^2}{\Delta t} \right\rangle$$

$$= \frac{1}{2} \left[\left\langle \frac{(\Delta J_x^b)^2}{\Delta t} \right\rangle (1 + \cos^2\theta) + \left\langle \frac{(\Delta J_z^b)^2}{\Delta t} \right\rangle \sin^2\theta \right], \tag{64}$$

$$B_{zz}^J \equiv \left\langle \frac{(\Delta J_z)^2}{\Delta t} \right\rangle$$

$$= \left[\left\langle \frac{(\Delta J_z^b)^2}{\Delta t} \right\rangle \cos^2\theta + \left\langle \frac{(\Delta J_y^b)^2}{\Delta t} \right\rangle \sin^2\theta \right], \tag{65}$$

and $B_{yy}^J = B_{xx}^J$.

Equations (61)–(71) can be used to find the diffusion coefficients in the $\boldsymbol{J}$-frame for an arbitrary interaction process. For gas–grain collisions, we get $\tau_1 = \tau_{\rm gas,1}$ and $\tau_2 = \tau_{\rm gas,2}$, which are $\tau_{\rm H,\parallel}$ and $\tau_{\rm H,\perp}$ for a purely hydrogen atomic gas.

For IR emission, recall that $\Delta J_{\rm IR,i}^b / \Delta t = -J_i^b / \tau_{\rm IR,i}$. Then, $\tau_1 = \tau_{\rm IR,1}$ and $\tau_2 = \tau_{\rm IR,2}$, where $\tau_{\rm IR,i}^{-1} = F_{\rm IR,i} \tau_{\rm gas,i}^{-1}$. Thus, we can get the IR damping in the $\boldsymbol{J}$-frame,

$$\left\langle \frac{\Delta J_{\rm IR,z}}{\Delta t} \right\rangle = -\frac{J_z}{\tau_{\rm IR,eff}} = -\frac{J_z}{\tau_{\rm eff}} \times F_{\rm IR,1}, \tag{66}$$

where

$$\tau_{\rm IR,eff} = F_{\rm IR,1}^{-1} \tau_{\rm gas,1} \epsilon_{\rm IR}(\theta), \quad \epsilon_{\rm IR}(\theta) = \frac{1}{\cos^2\theta + \gamma_{\rm IR} \sin^2\theta},$$

$$\gamma_{\rm IR} = \frac{\tau_{\rm IR,1}}{\tau_{\rm IR,2}} = \frac{\tau_{\rm gas,1}}{\tau_{\rm gas,2}} \times \frac{F_{\rm IR,2}}{F_{\rm IR,1}}, \tag{67}$$

for a simultaneous transformation of all damping processes with individual timescales τ_i. Then, we have the total rate of damping: $\tau_{\rm tot,1}^{-1} = \sum_{i=n,{\rm ion},p,{\rm IR}} \tau_{i,1}^{-1} = \left(\sum_i F_{i,1}\right) \tau_{\rm gas,1}^{-1} = F_{\rm tot,1} \tau_{\rm gas,1}^{-1}$, and $\tau_{\rm tot,2}^{-1} = \sum_{i=n,{\rm ion},p,{\rm IR}} \tau_{i,2}^{-1} = \left(\sum_i F_{i,2}\right) \tau_{\rm gas,2}^{-1} = F_{\rm tot,2} \tau_{\rm gas,2}^{-1}$. Thus, the total damping rate in the $\boldsymbol{J}$-system is

$$A_z^J \equiv \left\langle \frac{\Delta J_z}{\Delta t} \right\rangle = -\frac{J_z}{\tau_{\rm tot,eff}}, \quad A_{x,y}^J = \left\langle \frac{\Delta J_{x,y}}{\Delta t} \right\rangle = 0, \tag{68}$$

where $\tau_{\rm tot,eff} = \tau_{\rm tot,1} \epsilon_{\rm tot}$. Following Equation (62), it yields

$$\tau_{\rm tot,eff} = \tau_{\rm gas,1} F_{\rm tot,1}^{-1} \epsilon_{\rm tot}, \quad \epsilon_{\rm tot}(\theta) = \frac{1}{\cos^2\theta + \gamma_{\rm tot} \sin^2\theta}, \quad \gamma_{\rm tot}$$

$$= \frac{\tau_{\rm tot,1}}{\tau_{\rm tot,2}} = \frac{\tau_{\rm gas,1}}{\tau_{\rm gas,2}} \times \frac{F_{\rm tot,2}}{F_{\rm tot,1}}. \tag{69}$$

Let $B_{{\rm tot},ii}^b = \sum_{j=n,p,{\rm ion},{\rm IR}} B_{j,ii}^b$ be the total diffusion coefficients from the various processes in the body frame. The total diffusion coefficients in the $\boldsymbol{J}$-frame then can be given by Equation (71), but with

$$B_{xx}^J \equiv \left\langle \frac{(\Delta J_{x,y})^2}{\Delta t} \right\rangle = \frac{1}{2} [B_{{\rm tot},xx}^b (1 + \cos^2\theta) + B_{{\rm tot},zz}^b \sin^2\theta], \tag{70}$$

$$B_{zz}^J \equiv \left\langle \frac{(\Delta J_z)^2}{\Delta t} \right\rangle = [B_{{\rm tot},zz}^b \cos^2\theta + B_{{\rm tot},yy}^b \sin^2\theta], \tag{71}$$

and $B_{yy}^J = B_{xx}^J$. Note that the diffusion coefficients are proportional to the excitation coefficients:

$$B_{zz}^b = G_{zz} \left(\frac{2 I_1 k T_{\rm gas}}{\tau_{\rm gas,1}} \right), \quad B_{xx}^b = G_{xx} \left(\frac{2 I_2 k T_{\rm gas}}{\tau_{\rm gas,2}} \right), \tag{72}$$

where G_{xx} and G_{zz} are calculated in the grain-body system. The diffusion and excitation coefficients are defined by energy, so

they are additive. In dimensionless units, we have (see also Hoang & Lazarian 2016a)

$$B_{zz}^{\prime b} = B_{zz}^{b}\left(\frac{\tau_{\text{gas},1}}{2I_1 k T_{\text{gas}}}\right) = G_{zz}, \quad B_{xx}^{\prime b}$$

$$= B_{xx}^{b}\left(\frac{\tau_{\text{gas},1}}{2I_1 k T_{\text{gas}}}\right) = G_{xx}\left(\frac{\tau_{\text{gas},1}}{h_a \tau_{\text{gas},2}}\right). \tag{73}$$

A.3.2. J-frame to B-frame and Averaging over the Larmor precession

Since $A_{x,y} = 0$, following Equation (71), the damping coefficient is directly given by

$$A_{x,y,z} = -\frac{J_{x,y,z}}{\tau_{\text{tot,eff}}}. \tag{74}$$

The transformation of the diffusion coefficients from J-frame to B-frame is equivalent to the transformation from body frame to J-frame, where θ, ζ in Equations (64) and (65) will be replaced by ξ and ϕ. Therefore, we get

$$B_{zz} = B_{\parallel}\left(\frac{1}{2}\sin^2\theta\sin^2\xi + \cos^2\theta\cos^2\xi\right)$$
$$+ B_{\perp}\left(\frac{1}{2}[1 + \cos^2\theta]\sin^2\xi + \sin^2\theta\cos^2\xi\right),$$

$$B_{xx} = B_{\parallel}\left(\frac{1}{2}\sin^2\theta[\cos^2\phi + \sin^2\phi\cos^2\xi] + \cos^2\theta\sin^2\phi\sin^2\xi\right)$$
$$+ B_{\perp}\left(\frac{1}{2}[1 + \cos^2\theta][\cos^2\phi + \sin^2\phi\cos^2\xi]\right.$$
$$\left.+ \sin^2\theta\sin^2\phi\sin^2\xi\right),$$

$$B_{yy} = B_{\parallel}\left(\frac{1}{2}\sin^2\theta[\sin^2\phi + \cos^2\phi\cos^2\xi] + \cos^2\theta\sin^2\phi\sin^2\xi\right)$$
$$+ B_{\perp}\left(\frac{1}{2}[1 + \cos^2\theta][\sin^2\phi + \cos^2\phi\cos^2\xi]\right.$$
$$\left.+ \sin^2\theta\sin^2\phi\sin^2\xi\right),$$

where ξ is the angle between J and $\hat{z}_B$, and ϕ is the azimuthal angle of J in the inertial system $\hat{z}_i$ (see Figure 2). The Larmor precession averaging over ϕ gives $\langle\cos^2\phi\rangle = \langle\sin^2\phi\rangle = 1/2$, so that the diffusion coefficients return to those obtained in Lazarian (1997b).

Appendix B
Thermal Dust Emission

The intensity of thermal dust emission from dust grains in an optically thin diffuse region can be approximated by

$$I_{\text{td}} \sim B_\nu(T_d)\tau_\nu = B_\nu(T_d)\kappa(\nu)N_{\text{H}}, \tag{75}$$

where T_d is the grain equilibrium temperature that scales with the radiation intensity as $U^{1/5.67}$, and

$$\kappa(\nu) = 0.92 \times 10^{-25}\left(\frac{\lambda}{250\,\mu\text{m}}\right)^{-1.8}$$
$$\sim 10^{-27}\left(\frac{\nu}{100\,\text{GHz}}\right)^{1.8}\text{cm}^2\,\text{H}^{-1} \tag{76}$$

is the dust opacity per H at long wavelengths (Planck Collaboration et al. 2011). Therefore, one obtains

$$\frac{I_{\text{td}}}{N_{\text{H}}} \simeq 6.1 \times 10^{-18}\left(\frac{\nu}{100\,\text{GHz}}\right)^{3.8}\left(\frac{T_d}{20\,\text{K}}\right)$$
$$\times\text{Jy sr}^{-1}\,\text{cm}^2\,\text{H}^{-1}. \tag{77}$$

The polarization of thermal dust emission is observed by Planck Collaboration et al. (2015b), which has the maximum polarization fraction of 20% for the diffuse cloud and decreases with increasing N_{H}. For thermal dust emissivity shown in the present paper, we adopt $T_d = 20$ K for the CNM and $T_d = 60$ K for the RNe and PDRs. The polarization fraction is fixed at 20%.

ORCID iDs

Thiem Hoang ⓘ https://orcid.org/0000-0003-2017-0982

References

Allamandola, L. J., Tielens, A. G. G. M., & Barker, J. R. 1985, ApJL, 290, L25
Barnett, S. J. 1915, PhRv, 6, 239
Battistelli, E. S., Carretti, E., Cruciani, A., et al. 2015, ApJ, 801, 111
Battistelli, E. S., Rebolo, R., Rubiño-Martín, J. A., et al. 2006, ApJL, 645, L141
Das, I., & Weingartner, J. C. 2016, MNRAS, 457, 1958
Davis, L. J., & Greenstein, J. L. 1951, ApJ, 114, 206
Dickinson, C., Peel, M., & Vidal, M. 2011, MNRAS, 418, L35
Dolginov, A. Z., & Mitrofanov, I. G. 1976, Ap&SS, 43, 291
Dolginov, A. Z., & Mytrophanov, I. G. 1976, Ap&SS, 43, 257
Draine, B. 1989, in IAU Symp. 135, Interstellar Dust, ed. L. Allamandola & A. Tielens (Dordrecht: Kluwer), 313
Draine, B. T., & Hensley, B. 2013, ApJ, 765, 159
Draine, B. T., & Hensley, B. S. 2016, ApJ, 831, 59
Draine, B. T., & Lazarian, A. 1998, ApJ, 508, 157
Draine, B. T., & Lazarian, A. 1999, ApJ, 512, 740
Draine, B. T., & Li, A. 2001, ApJ, 551, 807
Draine, B. T., & Li, A. 2007, ApJ, 657, 810
Génova-Santos, R., Rubiño-Martín, J. A., Peláez-Santos, A., et al. 2017, MNRAS, 464, 4107
Gold, T. 1952, Natur, 169, 322
González-Herrero, H., Gómez-Rodríguez, J. M., Mallet, P., et al. 2016, Sci, 352, 437
Greenberg, J. M. 1968, in Nebulae and Interstellar Matter, ed. M. Barbara, Middlehurst, & H. Lawrence (Chicago: Univ. Chicago Press), 221
Guhathakurta, P., & Draine, B. T. 1989, ApJ, 345, 230
Hensley, B. S., & Draine, B. T. 2017, ApJ, 836, 179
Hoang, T. 2017, ApJ, 838, 112
Hoang, T., Cho, J., & Lazarian, A. 2018a, ApJ, 852, 129
Hoang, T., Draine, B. T., & Lazarian, A. 2010, ApJ, 715, 1462
Hoang, T., Lan, N.-Q., Vinh, N.-A., & Kim, Y.-J. 2018b, ApJ, (arXiv:1803.11028)
Hoang, T., & Lazarian, A. 2008, MNRAS, 388, 117
Hoang, T., & Lazarian, A. 2012, ApJ, 761, 96
Hoang, T., & Lazarian, A. 2016a ApJ, 821, 91
Hoang, T., & Lazarian, A. 2016b ApJ, 831, 159
Hoang, T., Lazarian, A., & Draine, B. T. 2011, ApJ, 741, 87
Hoang, T., Lazarian, A., & Martin, P. G. 2013, ApJ, 779, 152
Hoang, T., Lazarian, A., & Martin, P. G. 2014, ApJ, 790, 6
Hoang, T., Lazarian, A., & Schlickeiser, R. 2012, ApJ, 747, 54
Hoang, T., Vinh, N. A., & Quynh Lan, N. 2016, ApJ, 824, 18
Jones, R. V., & Spitzer, L. 1967, ApJ, 147, 943
Kataoka, A., Tsukagoshi, T., Pohl, A., et al. 2017, ApJL, 844, L5
Kogut, A., Banday, A. J., Bennett, C. L., et al. 1996, ApJL, 464, L5
Lazarian, A. 1994, MNRAS, 268, 713
Lazarian, A. 1995a ApJ, 451, 660
Lazarian, A. 1995b MNRAS, 277, 1235
Lazarian, A. 1997a, ApJ, 483, 296
Lazarian, A. 1997b, MNRAS, 288, 609
Lazarian, A. 2003, JQSRT, 79, 881

Lazarian, A., Andersson, B.-G., & Hoang, T. 2015, in Polarimetry of Stars and Planetary Systems, ed. L. Kolokolova, J Hough, & A.-C. Levasseur-Regourd (New York: Cambridge Univ. Press), 81
Lazarian, A., & Draine, B. T. 2000, ApJL, 536, L15
Lazarian, A., & Efroimsky, M. 1996, ApJ, 466, 274
Lazarian, A., & Hoang, T. 2007a ApJL, 669, L77
Lazarian, A., & Hoang, T. 2007b MNRAS, 378, 910
Lazarian, A., & Hoang, T. 2008, ApJL, 676, L25
Lazarian, A., & Roberge, W. G. 1997, ApJ, 484, 230
Leger, A., & Puget, J.-L. 1984, A&A, 137, L5
Lehtinen, P. O., Foster, A. S., Ma, Y., Krasheninnikov, A. V., & Nieminen, R. M. 2004, PhRvL, 93, 187202
Leitch, E. M., Readhead, A. C. S., Pearson, T. J., & Myers, S. T. 1997, ApJL, 486, L23
Li, D., Pantin, E., Telesco, C. M., et al. 2016, ApJ, 832, 18
López-Caraballo, C. H., Rubiño-Martín, J. A., Rebolo, R., & Génova-Santos, R. 2011, ApJ, 729, 25
Mason, B. S., Robishaw, T., Heiles, C., Finkbeiner, D., & Dickinson, C. 2009, ApJ, 697, 1187
Mathis, J. S., Mezger, P. G., & Panagia, N. 1983, A&A, 128, 212

Planck Collaboration, Abergel, A., Ade, P. A. R., et al. 2011, A&A, 536, 21
Planck Collaboration, Ade, P. A. R., Aghanim, N., et al. 2015a, arXiv:1506.06660
Planck Collaboration, Ade, P. A. R., Aghanim, N., et al. 2015b, A&A, 576, A104
Purcell, E. M. 1976, ApJ, 206, 685
Purcell, E. M. 1979, ApJ, 231, 404
Roberge, W. G., & Lazarian, A. 1999, MNRAS, 305, 615
Rubiño-Martín, J. A., López-Caraballo, C. H., Génova-Santos, R., & Rebolo, R. 2012, AdAst, 2012, 351836
Sellgren, K., Rouan, D., & Leger, A. 1988, A&A, 196, 252
Seok, J. Y., & Li, A. 2017, ApJ, 835, 291
Sironi, L., & Draine, B. T. 2009, ApJ, 698, 1292
Smith, J.-D. T., Draine, B. T., Dale, D. A., et al. 2007, ApJ, 656, 770
Stephens, I. W., Yang, H., Li, Z.-Y., et al. 2017, ApJ, 851, 55
Tazaki, R., Lazarian, A., & Nomura, H. 2017, ApJ, 839, 56
Tielens, A. G. G. M. 2008, ARA&A, 46, 289
Vanden-Eijnden, E., & Ciccotti, G. 2006, CPL, 429, 310
Weingartner, J. C., & Draine, B. T. 2001, ApJ, 548, 296
Yazyev, O. V., & Helm, L. 2007, PhRvB, 75, 125408
Zhang, H., Telesco, C. M., Hoang, T., et al. 2017, ApJ, 844, 6